

A CENSUS OF STARS AND DISKS IN CORONA AUSTRALIS<sup>1</sup>T. L. ESPLIN<sup>2</sup> AND K. L. LUHMAN<sup>3,4</sup>*Draft version December 1, 2021*

## ABSTRACT

We have performed a census of the young stellar populations near the Corona Australis molecular cloud using photometric and kinematic data from several sources, particularly Gaia EDR3, and spectroscopy of hundreds of candidate members. We have compiled a catalog of 393 members of Corona Australis, (39 at  $>M_6$ ), 293 (36) of which are spectroscopically classified for the first time in this work. We find that Corona Australis can be described in terms of two stellar populations, a younger one (few Myr) that is partially embedded in the cloud (the Coronet Cluster) and an older one ( $\sim 15$  Myr) that surrounds and extends beyond the cloud (Upper Corona Australis). These populations exhibit similar space velocities, and we find no evidence for distinct kinematic populations in Corona Australis, in contrast to a recent study based on Gaia DR2. The distribution of spectral types in Corona Australis reaches a maximum at M5 ( $\sim 0.15 M_\odot$ ), indicating that the IMF has a similar characteristic mass as other nearby star-forming regions. Finally, we have compiled mid-infrared photometry from the Wide-field Infrared Survey Explorer and the Spitzer Space Telescope for the members of Corona Australis and we have used those data to identify and classify their circumstellar disks. Excesses are detected for 122 stars, a third of which are reported for the first time in this work.

*Subject headings:* accretion disks - brown dwarfs - protoplanetary disks - stars: formation - stars: low-mass - stars: pre-main sequence

## 1. INTRODUCTION

Identifying a well-defined sample of the members of a young stellar association is required to measure many of its fundamental properties, which can provide insight into the processes of star and planet formation. A few such measurements include the distribution of masses of the stellar and substellar members (i.e., the initial mass function; IMF) and the frequency of disk-bearing members. The minimum mass of the former can be used to test theories of star formation (Whitworth et al. 2007, references therein) and the latter constrains the time available for giant planet formation (e.g., Mamajek 2009).

Corona Australis is among the nearest star-forming regions ( $\sim 149$  pc, Neuhäuser & Forbrich 2008; Galli et al. 2020), making it feasible to perform a census of its members down to planetary masses ( $\lesssim 15 M_{\text{Jup}}$ ). Based on early surveys, the region appeared to consist of a young embedded population, the Coronet Cluster (Meyer & Wilking 2009; Nisini et al. 2005; Sicilia-Aguilar et al. 2011) and a less obscured distribution of stars surrounding the molecular cloud that may have older ages (Peterson et al. 2011; Cazzoletti et al. 2019). The high-precision astrometry from the Gaia mission (Perryman et al. 2001; Gaia Collaboration et al. 2016) has recently

provided new measurements of the kinematic structure of Corona Australis. In the first data release of Gaia, Gagné et al. (2018) discovered a group of 10 stars between Corona Australis and the Scorpius-Centaurus OB association and near the distance of both regions, which they named Upper Corona Australis. Using the second data release of Gaia (DR2, Gaia Collaboration et al. 2018), Galli et al. (2020) identified many more candidate members of that new population and found that it is kinematically distinct from and slightly older than the stars near the Corona Australis molecular cloud. However, the characterization of these stellar populations has been limited by the fact that only a small fraction of the candidate members have been observed with spectroscopy, which is necessary for measuring spectral types and confirming youth.

We have performed a census of the members of the stellar populations near Corona Australis using astrometry, photometry, and spectroscopy from a variety of sources. We begin by characterizing the kinematics of the young stars projected against the Corona Australis cloud using the early installment of the third data release of Gaia (EDR3; Gaia Collaboration et al. 2021) (Section 2). We compile objects that have confirmation of youth and that satisfy our kinematic criteria for membership (Section 3) and we identify new candidate members via their proper motions, parallaxes, and photometry (Section 4). We present optical and infrared (IR) spectroscopy for a large number of candidates to measure their spectral types and assess their youth (Section 5). For stars that are adopted as members of Corona Australis, we characterize their space velocities, relative ages, and IMF and we check for the presence of circumstellar disks (Section 6).

<sup>1</sup> Based on observations made with the Gaia mission, the Two Micron All Sky Survey, the Wide-field Infrared Survey Explorer, the Spitzer Space Telescope, the NASA Infrared Telescope Facility, Cerro Tololo Inter-American Observatory, and Magellan Observatory.

<sup>2</sup> Steward Observatory, University of Arizona, Tucson, AZ, 85719, USA; taranesplin@email.arizona.edu

<sup>3</sup> Department of Astronomy and Astrophysics, The Pennsylvania State University, University Park, PA 16802; taran.esplin@psu.edu

<sup>4</sup> Center for Exoplanets and Habitable Worlds, The Pennsylvania State University, University Park, PA 16802.

## 2. KINEMATICS OF YOUNG STARS TOWARD CORONA AUSTRALIS

### 2.1. Kinematic Populations from Galli et al. (2020)

The proper motions and parallaxes for young stars toward Corona Australis have been examined previously by Galli et al. (2020). In that study, candidate members of the region were identified using a Gaussian mixture model (GMM) that was applied to proper motions and parallaxes ( $\mu_\alpha$ ,  $\mu_\delta$ ,  $\pi$ ) from Gaia DR2 and a second statistical model that was applied to the Gaia photometry. The Bayesian information criterion (BIC) favored a two component model, which was interpreted as evidence that Corona Australis was composed of two kinematically distinct populations. Most members of two populations had  $b \lesssim -16^\circ$  and  $b \gtrsim -16^\circ$ , which they referred to as on- and off-cloud, respectively.

The proper motion that corresponds to a given space velocity varies with position on the sky due to projection effects. To investigate the influence of projection effects on the results of Galli et al. (2020), we have plotted the two populations from that study in Figure 1 on diagrams of proper motions versus parallax and proper motion offsets ( $\Delta\mu_\alpha$ ,  $\Delta\mu_\delta$ ) versus parallax using data from Gaia EDR3. We have included density contours for each set of data. Projection effects are reduced in proper motion offsets, which are defined as the difference between the observed proper motion and the motion expected at a given source’s celestial coordinates and parallax if it has a specified space velocity (Luhman 2018; Esplin & Luhman 2019, 2020; Luhman & Esplin 2020). We have calculated the offsets assuming  $U$ ,  $V$ ,  $W$ , =  $-6, -17, -8$  km s $^{-1}$ , which was the median velocity for a preliminary sample of members prior to our spectroscopic survey. The median velocity of our final sample of members is  $-3.9$ ,  $-17.4$ , and  $-9.3$  km s $^{-1}$  (Section 6.1). If the proper motion offsets were calculated using the latter velocity, they would shift by a value that is very small and nearly constant for all members, and thus would have no effect on our results.

In Figure 1, two maxima are present in  $\mu_\alpha$  versus  $\pi$ , which correspond to the two populations from Galli et al. (2020). However, the candidates collapse into a single cluster in  $\Delta\mu_\alpha$  versus  $\pi$ , where projection effects are minimized. Projection effects across Corona Australis lead to a broadening primarily in  $\mu_\alpha$ , and a minimum in the surface density of the members near  $b \sim -16^\circ$  results in two maxima in  $\mu_\alpha$  instead of a single elongated distribution, and hence the identification of two apparent populations by Galli et al. (2020). Meanwhile, in  $\Delta\mu_\alpha$  versus  $\pi$ , the two populations from Galli et al. (2020) comprise two halves of the single cluster, which is due to the fact that  $\Delta\mu_\alpha$  is correlated with Galactic latitude among these stars and the two populations can be largely divided by latitude. As an additional comparison of the kinematics of the two samples from Galli et al. (2020), we have calculated the  $UVW$  velocities for the stars that have measurements of parallaxes and radial velocities (Section 6.1). The resulting velocities are shown in Figure 2. In each pair of velocities, the two samples together form a single cluster, and there is no evidence of separate populations. The two samples do have systematically different velocities in  $W$ , which is a reflection of the different latitudes for the two samples and the correlation between  $W$  and latitude among these stars (also manifested in the correlation between  $\Delta\mu_\alpha$  and latitude).

### 2.2. Corona Australis in Gaia EDR3

We have used data from Gaia EDR3 to characterize the kinematics of young stars near the Corona Australis cloud. We have selected sources from Gaia EDR3 with right ascensions between  $275$  and  $288.5^\circ$ , declinations between  $-40$  and  $-32.5^\circ$ , parallaxes of  $5.5$ – $8.5$  mas,  $\sigma_\pi/\pi \leq 0.1$ , and renormalized unit weight errors  $> 1.6$  (RUWEs, Lindegren 2018). The resulting sample is plotted in a diagram of  $M_{G_{\text{RP}}}$  versus  $G_{\text{BP}} - G_{\text{RP}}$  in Figure 3. These bands cover  $3300$ – $6800$  Å ( $G_{\text{BP}}$ ) and  $6300$ – $10500$  Å ( $G_{\text{RP}}$ ). The third Gaia band spans from  $3300$ – $10500$  Å ( $G$ ). We have included the single star sequence for the Tuc-Hor association (45 Myr, Bell et al. 2015) from Luhman & Esplin (2020). We have selected the sources appearing above that sequence between  $G_{\text{BP}} - G_{\text{RP}} = 1.4$ – $3.4$  as candidates for young low-mass stars.

In the left panel of Figure 4, we have plotted  $\Delta\mu_\alpha$  and  $\Delta\mu_\delta$  versus  $\pi$  for the CMD-selected candidates that have  $|\Delta\mu| < 10$  mas yr $^{-1}$ . Most of the candidates are tightly clustered in those diagrams, which correspond to members of Corona Australis. To separate the members from the small number of unclustered field stars, we have applied GMMs to the proper motion offsets and parallaxes using the `mclust` library in R (Scrucca et al. 2016; R Core Team 2017). The models consist of a noise component for the field stars and 1–4 Gaussian components. The noise component was initialized using the nearest-neighbor cleaning method from Byers & Raftery (1998) implemented in the `prabcus` library (Hennig & Hausdorf 2019). We found that two components (plus noise) were statistically preferred according to the BIC. However, the two components are indistinguishable in terms of their spatial distributions (Figure 4), ages, and extinctions (Section 6.2), which suggests that they do not comprise physically distinct populations. Meanwhile, the two components overlap to a large extent in the kinematic parameters that were fit by the GMM (Figure 4), and thus could easily represent a single kinematic population that has non-Gaussian distributions in proper motion offsets and parallax. Such non-Gaussian distributions have been observed for populations in other star-forming regions and associations (Luhman & Esplin 2020).

## 3. CATALOG OF KNOWN MEMBERS OF CORONA AUSTRALIS

We have compiled stars within the survey field encompassing Corona Australis from Section 2.2 that have evidence of youth from previous studies or this work (Section 4) and that are not rejected as non-members by available measurements of proper motions and parallaxes. We have identified stars that have evidence of youth, parallaxes from Gaia EDR3 with errors less than  $0.5$  mas, and  $\Delta\mu_\alpha$ ,  $\Delta\mu_\delta$ , and  $\pi$  that overlap at  $1\sigma$  with the  $2\sigma$  ellipses of the GMM components in Figure 4, which results in 347 objects that are adopted as members. We also have assigned membership to 13 stars that have  $\sigma_\pi < 0.5$  mas and do not satisfy the preceding kinematic criteria, consisting of two objects that are candidate companions to adopted members (Gaia EDR3 6730717024217228928, 2MASS J19104337–3659092) and nine sources that may have unreliable astrometry based on values of RUWE greater than  $1.6$ . In addition, we have adopted 33 stars that lack

parallaxes with  $\sigma_\pi < 0.5$  mas and have other data that support membership, many of which are protostars (Nutter et al. 2005). The combined catalog of 393 adopted members is presented in Table 1. Previous evidence of youth (primarily from spectra) is available for 100 stars and the remaining sources are spectroscopically classified for the first time in this work. The spatial distribution of the adopted members is illustrated in a map of their Galactic coordinates in Figure 5.

Table 1 contains source designations from the AllWISE Source Catalog of the Wide-field Infrared Survey Explorer (WISE, Wright et al. 2010) and the Point Source Catalog of the Two Micron All Sky Survey (2MASS, Skrutskie et al. 2006); additional names from the literature; spectral types from previous studies and this work; astrometry from Gaia EDR3; if  $\sigma_\pi < 0.5$  mas, a flag indicating whether the Gaia kinematic criteria for membership are satisfied; distance estimate based on the Gaia EDR3 parallax (Bailer-Jones et al. 2021); proper motions measured from IR images in Section 4.2; the most accurate available radial velocity measurement that has an error less than  $4 \text{ km s}^{-1}$ ;  $UVW$  velocities calculated from the radial velocity, proper motion, and parallactic distance; photometry in bands from Gaia EDR3, 2MASS, WISE, and the Spitzer Space Telescope; flags indicating whether excesses are detected in WISE and Spitzer bands; disk classification if excess emission is detected; and extinction estimates. The latter were derived from our near-IR spectra or  $J - H$  and  $J - K_s$  colors, as indicated in Table 1.

#### 4. IDENTIFICATION OF CANDIDATE MEMBERS

##### 4.1. Proper Motions and Parallaxes from Gaia EDR3

In Section 2.2, we characterized the proper motion offsets and parallaxes for Corona Australis using candidate young low-mass stars selected from a CMD. We now use those kinematics to define criteria for searching for candidate members of Corona Australis at all magnitudes and colors in Gaia EDR3. As in our compilation of adopted members in Section 3, we consider sources from EDR3 that have locations within the survey field from Section 2.2,  $\sigma_\pi < 0.5$  mas, and  $\Delta\mu_\alpha$ ,  $\Delta\mu_\delta$ , and  $\pi$  that overlap at  $1 \sigma$  with the  $2 \sigma$  ellipses of the GMM components in Figure 4. These criteria produce 346 objects that lack previous evidence of youth or spectral classifications, 311 of which have  $\text{RUWE} < 1.6$ . We recover all but nine of the 254 candidates identified by Galli et al. (2020), which consist of Gaia DR2 6728069984365602944, 6734711957980514432, 6736763921557552000, 6733973361050980352, 6733584275683948032, 6729972895366111232, 6730588072134320512, 6735323118961200000, and 6730960218154606464.

##### 4.2. Proper Motions from IR Imaging

To search for candidate members of Corona Australis that are too faint for Gaia parallax measurements, such as heavily embedded stars or low-mass brown dwarfs, we have measured proper motions of sources projected against the molecular cloud using multi-epoch IR imaging. The first set of data that we have employed was taken with the Infrared Array Camera on the Spitzer Space Telescope (IRAC; Fazio et al. 2004; Werner et al.

2004). IRAC operated in bands centered near 3.6, 4.5, 5.8, and  $8.0 \mu\text{m}$  ([3.6], [4.5], [5.8], [8.0]) during its cryogenic phase, which was from August 2003 through May 2009. It then collected data in only the first two bands for the remainder of the mission. The images from IRAC had a plate scale of  $1''.2 \text{ pixel}^{-1}$  and a field of view of  $5'.2 \times 5'.2$ . The FWHM of point sources in [3.6]–[8.0] was  $1''.6$ – $1''.9$ .

We began by compiling all [3.6] and [4.5] images that encompass the Corona Australis molecular cloud. The Astronomical Observing Requests (AORs), program identifications (PIDs), and principle investigators (PIs) of the observations are listed in Table 2. These data have primarily been used to classify the circumstellar disks of previously known members of the cloud (Sicilia-Aguilar et al. 2008; Currie & Sicilia-Aguilar 2011; Peterson et al. 2011). The IRAC images were obtained at four epochs that span 8.6 years. The exposure time for individual images was 10.4 s. For each of the first three epochs, two exposures were taken in each of the two bands for a given position. In the fourth epoch, nine images were obtained in each band. In Figure 6, we have plotted a map with the fields encompassed by the four epochs of IRAC imaging.

We have measured astrometry for the sources in the IRAC images in [3.6] and [4.5] using the methods developed in Esplin & Luhman (2016) and Esplin et al. (2017). First, the pixel positions, fluxes ( $F_\nu$ ), and signal-to-noise ratios (S/Ns) for every source were measured using the point-response-function fitting routine in the Astronomical Point source Extractor (APEX; Makovoz & Marleau 2005). We ignored sources with less than three detections from among all [3.6] and [4.5] exposures in a given epoch and sources that were close to saturation, as indicated by  $F_\nu/(\text{exposure time}) > 0.73$  and  $> 0.82 \text{ Jy s}^{-1}$  in [3.6] and [4.5], respectively. The pixel positions of the retained sources were corrected for distortion. Next, we estimated the central world coordinates and orientations of the fourth epoch of images using astrometry from Gaia DR2 when available, and otherwise used data from the sixth data release (DR6) of the Visible and Infrared Survey Telescope for Astronomy (VISTA) Hemisphere Survey (VHS, McMahon et al. 2013). We iteratively calculated a catalog of average positions of each source from the individual detections and updated the central coordinates and orientations using the new catalog. The orientations and central coordinates of the first three epochs were measured using the catalog of average positions in the fourth epoch.

Our proper motion calculations also made use of astrometry from near-IR images that we obtained with FourStar on the Magellan I Telescope at Las Campanas Observatory (Persson et al. 2013). FourStar contains four arrays with plate scales of  $0''.159 \text{ pixel}^{-1}$  arranged in a square with a total field of view of  $10'.8 \times 10'.8$ . We imaged the Coronet Cluster at  $J$  and  $H$  with four pointings on 2018 April 3, as shown in Figure 6. Each pointing consisted of 5/18 dithered images with individual exposure times of 64/5.8 s for  $J/H$ . The images were flat-field corrected and combined, and sources in the resulting images were identified using routines within IRAF. The average FWHM of point sources in the reduced images was  $1''.1$ . The completeness limits of the images were  $J = 20.5$  and

$H = 19.25$ , which are fainter than the limits from IRAC for the typical colors of young brown dwarfs. For every combined image in a given array, we fit fifth order polynomials to correct for distortion using astrometry from Gaia DR2.

Relative proper motions were measured from the multiple epochs of astrometry measured with IRAC and FourStar using a linear fit of right ascension and declination as a function of time. Because of the longer baseline from the combination of IRAC and FourStar (available only for the Coronet Cluster) relative to the IRAC epochs alone, the proper motion uncertainties from the former are smaller. For instance, objects with  $J = 14/17$  have typical errors of  $2.3/8.0 \text{ mas yr}^{-1}$  for IRAC+FourStar and  $3.5/16.5 \text{ mas yr}^{-1}$  for IRAC alone. We restrict our analysis to measurements with  $\sigma_\alpha$  and  $\sigma_\delta < 10 \text{ mas yr}^{-1}$ . We have measured IR proper motions for 49 of the adopted members of Corona Australis in Table 1, 28 of which have previous spectral classifications and 21 of which are newly classified in this work. Those motions are included in Table 1. We also have plotted the motions of those members and all other sources in our proper motion catalog in Figure 7. The members are well-separated from most other sources and have a median motion of  $(\mu_\alpha, \mu_\delta) = (3.75, -22.47) \text{ mas yr}^{-1}$ .

We have used the IR proper motions to identify candidate members of Corona Australis. We selected objects with proper motions within  $1 \sigma$  of a  $4 \text{ mas yr}^{-1}$  radius from the median motion of known members, which is shown in Figure 7. This threshold was selected because it is large enough to recover most of the previously known members. This criterion produces 241 objects that lack previous spectra, most of which do not satisfy the photometric criteria in the next section. All adopted members in Table 1 that have IR proper motions satisfy the criterion with the exception of CrA-26. The latter is projected against the molecular cloud and has high enough extinction that it is unlikely to be in the foreground of the cloud. Its proper motion from Gaia is more accurate than the IR measurements and is discrepant by only  $1.5 \sigma$ , so we have adopted it as a member.

#### 4.3. Color-magnitude Diagrams

To refine the kinematic candidates identified with Gaia and IR imaging and to select additional candidates that lack kinematic data, we have utilized several CMDs constructed from optical and IR photometry. We have made use of photometry from Gaia EDR3 ( $G$ ), VHS DR6 ( $J$  and  $K$ ), 2MASS ( $J$ ,  $H$ ,  $K_s$ ), AllWISE (W1 and W2), FourStar ( $J$  and  $H$ ), and IRAC ([3.6]). Offsets were applied to the VHS photometry to align it to the 2MASS data in the manner described by Luhman & Esplin (2020). Data from Gaia, VHS, and 2MASS are available for the entire survey field. The areas imaged by FourStar and IRAC are shown in Figure 6. In addition, we obtained  $z$ -band images of the Coronet Cluster with the Inamori Magellan Areal Camera and Spectrograph (IMACS, Dressler et al. 2011) on the Magellan I telescope on 2018 April 4. The instrument was operated in the f/2 mode, which produces a plate scale of  $0''.20 \text{ pixel}^{-1}$  and a circular field of view with a diameter of  $15'$ . The observations consisted of five dithered 150 s exposures. The average FWHM for point sources in the

IMACS images was  $1''$ .

To merge the catalogs of photometry, we identified all matching sources and adopted the photometry with the smallest errors when multiple similar bands were available. In our analysis, we have omitted photometry with  $\sigma > 0.1 \text{ mag}$ . To enable the construction of extinction-corrected CMDs, we estimated the extinction for each source using near-IR photometry in the manner done in our previous surveys of star-forming regions (Esplin et al. 2017, references therein). The data in the CMDs were then corrected for extinction using the reddening relations of Schlafly et al. (2016) and Indebetouw et al. (2005).

In Figure 8, we show the six extinction-corrected CMDs that we used to identify candidate members of Corona Australis. In each CMD, we have indicated a boundary that follows the lower envelope of the sequence of known members. We selected objects as photometric candidates if they appeared above a boundary in at least one CMD and were not below a boundary in any CMD. Among the 346 Gaia kinematic candidates from Section 4.1, 311 satisfy the CMD criteria. In Section 4.2, we identified 241 proper motion candidates from IR imaging that lack previous spectra, 13 of which are also among the Gaia kinematic candidates. Among the remaining 228 IR proper motion candidates, 22 satisfy the CMDs.

### 5. SPECTROSCOPY OF CANDIDATE MEMBERS

#### 5.1. Observations

We obtained optical and/or near-IR spectra of the most promising candidate members of Corona Australis to measure their spectral types and assess their youth. Highest priority was given to candidates that are located within the FourStar and IRAC fields (regardless of whether kinematic data were available) and candidates at any location in the full survey field that have kinematic data from Gaia. We also observed a small sample of stars that have spectral classifications from previous studies. The spectroscopic sample contains a total of 365 objects, which consist of 42 stars with previous classifications that are among our adopted members in Table 1, 293 new members that are spectroscopically classified as young for the first time in this work, and 30 sources that are non-members based on either their spectra or kinematics. Some of the latter were observed before data from Gaia DR2 and EDR3 became available. Several objects were observed with both optical and IR spectrographs.

The spectra were collected with the Cerro Tololo Ohio State Multi-Object Spectrograph (COSMOS), which is based on an instrument described by Martini et al. (2011), and the Astronomy Research using the Cornell Infra-Red Imaging Spectrograph (ARCoIRIS; Schlawin et al. 2014) on the 4 m Blanco telescope at Cerro Tololo Inter-American Observatory (CTIO); the Folded-port InfraRed Echellette (FIRE; Simcoe et al. 2013) on Magellan I at Las Campanas Observatory; the Gemini Multi-Object Spectrograph (GMOS; Hook et al. 2004) and FLAMINGOS-2 on the Gemini South Telescope (Eikenberry et al. 2004); and SpeX (Rayner et al. 2003) at the NASA Infrared Telescope Facility (IRTF). The instrument configurations, dispersers, wavelength coverages, and resolutions are summarized in Table 3. The observa-

tion dates for the individual targets are listed in Table 4.

The optical spectra from COSMOS and GMOS was reduced using routines in IRAF. We applied a flat field correction to the images, extracted the spectra, and performed the wavelength calibration using arc lamp spectra. The IR spectra from SpeX and ARCoIRIS were reduced using the Spextool package (Cushing et al. 2004) and a modified version of Spextool, respectively. Spextool corrects for telluric absorption in the manner described by Vacca et al. (2003). The FIRE and FLAMINGOS-2 data were processed with steps similar to those in Spextool using routines in R and IRAF, respectively. We present examples of the optical and IR spectra in Figures 9 and 10, respectively. The reduced spectra are provided in electronic files associated with those figures.

### 5.2. Spectral Classification

The photometry of our candidates indicates that they are likely to have K/M spectral types if they are members of Corona Australis. At those types, diagnostics of youth include Li I absorption at 6707 Å and gravity-sensitive features like the Na I double near 8190 Å and the H<sub>2</sub>O absorption bands at near-IR wavelengths (Martin et al. 1996; Luhman et al. 1997; Lucas et al. 2001). Spectroscopic evidence of youth is found for 340 of the 365 targets, which consist of 42 previously classified stars that are among our adopted members, 293 new members that are classified as young for the first time with our spectra, and five stars that are rejected as members based on their kinematics. As noted in the previous section, some of the spectroscopic targets classified as non-members would not satisfy our final selection criteria using Gaia EDR3. In Table 4, we indicate whether each object is classified as young and whether it is adopted as a member of Corona Australis.

In addition to assessing youth and membership, we have used our spectra to measure spectral types. Objects that lacked evidence of youth were classified through comparison to dwarf standards (Henry et al. 1994; Kirkpatrick et al. 1991, 1997; Cushing et al. 2005; Rayner et al. 2009). For the young stars, the optical spectra were classified with averages of dwarf and giant spectra (Luhman et al. 1997, 1998; Luhman 1999) and the IR spectra were classified with standard spectra constructed from optically classified young objects (Luhman et al. 2017). Our spectral classifications are included in the tabulation of our spectroscopic sample in Table 4. The catalog of adopted members of Corona Australis in Table 1 contains 39 objects with spectral types later than M6 ( $\lesssim 0.1 M_{\odot}$ , Baraffe et al. 1998), 36 of which have been classified for the first time in this work.

The most promising remaining candidates that lack spectral classifications consist of ten stars that satisfy our selection criteria for Gaia kinematics and CMDs (Sections 2.2 and 4.3) and have RUWE $<1.6$ . They are listed in Table 5. In addition, we have included in Table 5 two candidates identified with Gaia kinematics and CMDs that have RUWE $>1.6$  and 11 candidate companions to adopted members ( $< 2''$ ) that satisfy the CMDs but lack Gaia kinematic data. Based on their photometry, the first sample of 10 candidates should have spectral types that range from  $\sim$ K2 to M8.

## 6. PROPERTIES OF THE CORONA AUSTRALIS STELLAR POPULATION

### 6.1. Kinematics

In Table 1, we have included previous measurements of radial velocities that have errors less than 4 km s<sup>-1</sup>, which are available for 82 adopted members of Corona Australis. We have adopted an error of 0.4 km s<sup>-1</sup> for velocities from Torres et al. (2006) for which errors were not reported, which is near the typical precision estimated in that study. For the 72 stars with radial velocities and Gaia measurements of proper motions and parallaxes, we have used the radial velocities, proper motions, and parallactic distances (Bailer-Jones et al. 2021) to compute *UVW* space velocities (Johnson & Soderblom 1987), which are presented in Table 1. Errors in the space velocities were estimated using the radial velocity errors and the covariance matrices of errors and correlation coefficients for the Gaia astrometry (Brown et al. 1997). Among the 55 stars with *UVW* estimates,  $\sigma_{\pi} < 0.5$  mas, and RUWE $<1.6$ , the median velocity is  $U, V, W, = -3.9, -17.4, -9.3$  km s<sup>-1</sup>.

In the top row of Figure 11, we have plotted diagrams of Galactic Cartesian coordinates (*XYZ*) for adopted members with  $\sigma_{\pi} < 0.5$  mas and RUWE $<1.6$ . Those data indicate that the dimensions of Corona Australis range from 15–25 pc. In the bottom row of Figure 11, we show diagrams of *U*, *V*, and *W* versus *X*, *Y*, and *Z*, respectively, for the 55 stars with *UVW* estimates,  $\sigma_{\pi} < 0.5$  mas, and RUWE $<1.6$ . The stars exhibit a correlation between *W* and *Z*, which indicates expansion in that dimension, whereas correlations are not evident in the other two dimensions. In those diagrams of *UVW* versus *XYZ*, we have plotted stars with extinctions above and below  $A_J = 1$  with different symbols to compare the kinematics of the stars embedded in the molecular cloud and the remaining stars. The choice of  $A_J = 1$  is based on analysis in the next section. The two samples span similar ranges of *U*, *V*, and *W*. To expand the comparison of stars with low and high extinction to include those lacking radial velocity measurements, we have plotted the proper motion offsets and parallaxes for adopted members with  $\sigma_{\pi} < 0.5$  mas and RUWE $<1.6$  in Figure 12. One symbol is used for stars with  $A_J > 1$  and  $b < -17.3^\circ$ , which are likely embedded in the cloud, and a second symbol is used for all other stars. As in the *UVW* data, the embedded stars fall within the range of proper motion offsets and parallaxes exhibited by the less obscured members.

### 6.2. Relative Ages

As discussed in Section 1, the Coronet Cluster within the Corona Australis cloud appears to have an age of a few Myr (e.g., Meyer & Wilking 2009) while evidence has been reported for the presence of older stars in the vicinity of the cloud. For example, Cazzoletti et al. (2019) found that a sample of candidate members exhibited a distribution of dust masses that resembled that of Upper Sco, which has an age of  $\sim 10$  Myr (Pecaut et al. 2012; Pecaut & Mamajek 2016; Luhman & Esplin 2020). Stars older than the Coronet Cluster also have been identified in an area surrounding the cloud (Neuhäuser et al. 2000; Peterson et al. 2011). Meanwhile, Galli et al. (2020) found a small difference in ages (5 vs. 6 Myr) between

stars near and far from the cloud among their candidate members identified with Gaia DR2 (Section 2).

We can place new constraints on the presence of systematic variations in age in Corona Australis using our new census. Low-mass stars are predicted to evolve mostly vertically in the Hertzsprung-Russell diagram (e.g., Baraffe et al. 1998), so we can estimate the relative ages of young stars using their deviations in absolute magnitudes from a fiducial sequence. In previous studies (Esplin et al. 2018; Esplin & Luhman 2020), we have performed analysis of this kind using diagrams of  $M_K$  versus spectral type, estimating the difference between the extinction-corrected  $M_K$  of a given star and the median sequence for Upper Sco, which is denoted by  $\Delta M_K$ . We have applied this method to the K5–M5 stars in our census of Corona Australis. For stars with  $\sigma_\pi < 0.5$  mas and RUWE < 1.6, we have calculated  $M_K$  using the parallactic distances from Bailer-Jones et al. (2021). For the remaining stars, we have adopted the median distance of members with  $\sigma_\pi < 0.5$  mas and RUWE < 1.6 at  $b < -17.3^\circ$ , which is where most of the stars lacking accurate parallaxes are located.

We have examined the variation of  $\Delta M_K$  with celestial coordinates and extinction. We find that within an area toward the cloud, stars with extinctions above and below  $A_J \sim 1$  have systematically different  $\Delta M_K$ , which is illustrated in Figure 13, where we plot  $\Delta M_K$  versus  $A_J$  for members at  $b < -17.3^\circ$ . Therefore, we have divided the members of Corona Australis into three samples for the remaining analysis: stars near the cloud ( $b < -17.3^\circ$ ) with  $A_J > 1$  (concentrated in the Coronet Cluster), stars near the cloud ( $b < -17.3^\circ$ ) with  $A_J \leq 1$ , and stars farther from the cloud ( $b \geq -17.3^\circ$ ). Nearly all of the latter have  $A_J < 1$ . In Figure 14, we show a box-and-whisker diagram of the medians and interquartile ranges of  $\Delta M_K$  for those three samples. Errors in the medians were estimated via bootstrapping. We have indicated in Figure 14 the ages that correspond to  $\Delta M_K$  assuming an age of 10 Myr for Upper Sco and the luminosity evolution predicted by evolutionary models (Baraffe et al. 2015; Feiden 2016). The near-cloud  $A_J > 1$  stars exhibit a significantly younger median age ( $\sim 1$ –2 Myr) than the less obscured near-cloud stars ( $\sim 12$  Myr) and the off-cloud stars ( $\sim 15$  Myr). These results indicate that two populations are projected against the cloud, a younger one in which many of the members are embedded in the cloud and an older one surrounding the cloud. It is unclear whether the latter population is truly younger than the off-cloud stars as implied by Figure 14. It is possible that the young population associated with the cloud includes less-obscured members that contaminate the near-cloud  $A_J \leq 1$  sample, which could explain why the latter has a slightly younger median age than the off-cloud sample. The near-cloud  $A_J \leq 1$  sample and the off-cloud sample are sufficiently similar in age that we propose that they are both part of a single older population (approximated by members with  $A_J \leq 1$ ) that surrounds and extends beyond the cloud. Since some of the off-cloud stars have been previously referred to as “Upper Corona Australis” (Gagné et al. 2018; Galli et al. 2020), we adopt that name for the entire older population.

The Coronet Cluster and Upper Corona Australis resemble Ophiuchus and Upper Sco in terms of their relative numbers of stars, spatial distributions, kinematics,

and ages. In each region, 1) a population with an age of a few Myr is partially embedded within a molecular cloud and a population with an age of  $\gtrsim 10$  Myr surrounds the cloud and extends across a much larger area; 2) the cloud and its younger population are located near the edge of older population; 3) the older population is substantially richer; and 4) the older population spans a wider range of kinematics (proper motion offsets and  $UVW$ ) that largely encompasses the narrower range of kinematics of the younger population (Figures 11 and 12, Luhman 2021a).

### 6.3. Initial Mass Function

#### 6.3.1. Completeness

To analyze the IMF in Corona Australis, we begin by characterizing the completeness of our sample of adopted members within the field imaged by IRAC in two epochs or more and the field imaged by FourStar (Figure 6). We have constructed a CMD for the IRAC field using  $J$  and  $K_s$  from 2MASS and VHS and a CMD for the FourStar field using  $J$  and  $H$  from 2MASS and FourStar. These bands were chosen because they have the greatest sensitivity to brown dwarfs for these fields. In Figure 15, we show CMDs for the adopted members of Corona Australis in the IRAC and FourStar fields and the remaining sources that are not rejected by spectroscopy or any of the photometric and kinematic criteria in Section 4. For the IRAC and FourStar fields, there are no remaining sources with undetermined status down to extinction-corrected magnitudes of  $J = 15.6$  and 17, respectively, for  $A_J < 1$ . Assuming an age of 10 Myr, the median parallactic distance of the known members within the field, and the bolometric corrections from Filippazzo et al. (2015),  $J = 15.6$  and 17 should correspond to masses of  $\sim 0.02$  and  $\sim 0.015 M_\odot$ , respectively, according to evolutionary models (Burrows et al. 1997; Chabrier et al. 2000). For extinctions high enough to reach most members of the Coronet Cluster ( $A_J < 5$ ), the completeness limit is near an extinction-corrected magnitude of  $J = 14$  in the FourStar field, which corresponds to  $0.03$ – $0.04 M_\odot$  for ages of 1–3 Myr. When using Gaia EDR3 to search for members of Upper Sco, Luhman (2021a) found that the completeness was high among spectral types earlier than  $\sim M7$  for the low extinctions in the association ( $A_J < 1$ ). If we account for the differences in age and distance between Upper Sco and Corona Australis, then Gaia EDR3 should provide a completeness limit of  $\sim M6$  ( $\sim 0.1 M_\odot$ ) for our full survey field. Based on their photometry, roughly half of the 10 kinematic candidates with RUWE < 1.6 that lack spectra (Table 5) are expected to have types of  $\lesssim M6$ .

#### 6.3.2. Distribution of Spectral Types

As done in previous studies of nearby star-forming regions (e.g., Esplin & Luhman 2019), we have used spectral type as a proxy for stellar mass when characterizing the IMF of Corona Australis. In Figure 16, we show histograms of spectral type for the adopted members within the following four samples: 1)  $A_J \leq 1$  and within the field imaged by IRAC in multiple epochs, 2)  $A_J \leq 1$  and within our full survey field, 3)  $A_J \leq 1$  and within the FourStar field; and 4)  $A_J \leq 5$  and within the FourStar field. In each histogram, we have marked the

spectral type that corresponds to the completeness limit estimated in the previous section for that sample. The first two samples should be dominated by the members of the older population, Upper Corona Australis, due to the shallow extinction limits and the moderate-to-large sizes of the fields. For the third sample, the small field size favors members of the Coronet Cluster while the low extinction limit favors members of Upper Corona Australis. Since the fourth sample applies to the same small field but extends to higher extinction, it likely consists primarily of Coronet members. All of the histograms in Figure 16 exhibit a peak near M5 ( $\sim 0.15 M_{\odot}$ ), which is consistent with the distributions that we have measured in other star-forming regions (Luhman et al. 2016; Esplin & Luhman 2019; Luhman 2021a).

#### 6.4. Circumstellar Disks

##### 6.4.1. Mid-IR Photometry

To search for evidence of circumstellar disks among our adopted members of Corona Australis, we have compiled their mid-IR photometry from WISE and Spitzer. The WISE data were taken in bands centered at 3.4, 4.6, 12, and  $22 \mu\text{m}$  (W1–W4) and the Spitzer data were collected in the four bands of IRAC ([3.6]–[8.0]) and the  $24 \mu\text{m}$  band ([24]) of the Multiband Imaging Photometer for Spitzer (MIPS; Rieke et al. 2004). For each member, we searched for counterparts in the AllWISE Source Catalog and the WISE All-Sky Source Catalog. We adopted the data from the former when available (368 stars) and otherwise used the data from the latter (three stars). The WISE photometry is included in Table 1. For each member with a WISE counterpart, we visually inspected the WISE Atlas images to check for false or unreliable detections, blending with nearby sources, and contamination from extended emission, which are flagged in Table 1. Measurements with  $W2 < 6$  were excluded from our analysis because they are subject to large systematic errors (Cutri et al. 2012). Among the members with WISE counterparts, 98, 97, 84, and 24% have photometry at W1–W4, respectively.

A subset of the members of Corona Australis are encompassed by images obtained by IRAC and MIPS on Spitzer (Figure 6). When available, we retrieved photometry for members from the Spitzer Enhanced Imaging Products (SEIP) Source List. For members that were absent from SEIP but that were detected by Spitzer based on inspection of the images, we measured photometry from the SEIP mosaics in the manner described by Esplin et al. (2018). In Table 1, we present photometry for 109, 111, 92, 81, and 87 sources in [3.6], [4.5], [5.8], [8.0], and [24], respectively. All members encompassed by the IRAC images were detected in at least one band except for S CrA B, which was unresolved from its companion. Nine members fall within the MIPS images but were undetected or unresolved (including S CrA B).

##### 6.4.2. Disk Detections and Classifications

As done in our previous surveys (e.g., Esplin et al. 2018), we have used extinction-corrected colors between  $K_s$  and W2, W3, W4, [4.5], [8.0], and [24] to detect IR excesses from disks. For each color, we have subtracted the typical intrinsic value for a young stellar photosphere at the spectral type of a given star (Luhman 2021a). If

a star appears to exhibit an excess in a given band but a detection in any band at a longer wavelength is consistent with a photosphere, an excess is not assigned to the first band. In Table 1, we have included flags to indicate whether excesses are present in each of the six bands that we have considered. Excesses are detected for 122 adopted members of Corona Australis. The excesses for 41 stars have not been identified previously (Sicilia-Aguilar et al. 2008; Currie & Sicilia-Aguilar 2011; Peterson et al. 2011; Galli et al. 2020).

We have used the sizes of the IR excesses to classify the evolutionary stages of the disks according to the criteria that we have applied in previous studies (Luhman & Mamajek 2012; Esplin et al. 2014, 2018). Those stages consist of the following (Kenyon & Bromley 2005; Rieke et al. 2005; Hernández et al. 2007; Luhman et al. 2010; Espaillat et al. 2012): *full disks* are optically thick at mid-IR wavelengths with no large gaps or holes; *transitional disks* are optically thick with a large inner hole; *evolved disks* are optically thin and lack large gaps or holes; *evolved transitional disks* are optically thin with a large inner hole; and *debris disks* consist of second-generation dust produced by collisions of planetesimals. Debris and evolved transitional disks are indistinguishable in mid-IR photometry. In Table 1, we have listed the disk classifications for the 122 stars that exhibit IR excesses. We classify 76 as full (including nine previously identified protostars, Nutter et al. 2005; Forbrich et al. 2006), 15 as evolved, 28 as debris or evolved transitional, two as transitional, and one as evolved or transitional. In addition, we have appended “I” to the disk classifications in Table 1 for stars that have been previously classified as class I protostars.

##### 6.4.3. Disk Fractions

We have calculated the fraction of adopted members that have full, evolved, and transitional disks in each of the three samples defined for the age analysis in Section 6.2 for four ranges of spectral types that correspond roughly to logarithmic intervals of stellar mass (Baraffe et al. 1998). As done in our previous measurements of disk fractions, we have excluded protostars and evolved transitional disks. The resulting disk fractions are presented in Table 6. Several of the disk fractions have large uncertainties due to the small samples, but we can meaningfully compare the fractions for K6–M5.75, which offer the largest samples. For that range of types, the off-cloud, near-cloud  $A_J \leq 1$ , and near-cloud  $A_J > 1$  samples have disk fractions of  $0.14 \pm 0.03$ ,  $0.35^{+0.10}_{-0.08}$ , and  $0.61^{+0.25}_{-0.18}$ , respectively. The relative values of those fractions are consistent with the relative ages derived for those samples (i.e., the older samples have lower disk fractions). Similarly, the disk fraction of  $0.14 \pm 0.03$  for the off-cloud sample is between the K6–M5.75 disk fractions for Upper Sco ( $0.21^{+0.02}_{-0.01}$ ) and UCL/LCC ( $0.076 \pm 0.005$  Luhman 2021b), which is consistent with our age estimate for the off-cloud stars ( $\sim 15$  Myr) relative to the ages of Upper Sco and UCL/LCC ( $\sim 10$  and  $20$  Myr, Luhman & Esplin 2020).

## 7. CONCLUSION

We have performed a census of the young stellar populations near the Corona Australis molecular cloud using photometric and kinematic data from several sources,

particularly Gaia EDR3, and spectroscopy of hundreds of candidate members. We have used our new catalog of young stars to characterize the space velocities, relative ages, IMFs, and circumstellar disks in those populations. Our results are summarized as follows:

1. For our survey, we have considered a large area that extends well beyond the Corona Australis cloud ( $\alpha = 275$  to  $288.5^\circ$ ,  $\delta = -40$  to  $-32.5^\circ$ ). To characterize the kinematics of the young stellar populations within that field, we have identified a sample of young low-mass stars based on their positions in Gaia CMDs and we have applied a Gaussian mixture model to their proper motion offsets and parallaxes to separate the populations associated with the cloud from field stars. The kinematics of the model components for the former were then used as criteria for selecting candidate members from Gaia EDR3 at all magnitudes and colors. In addition, we have identified candidates based on proper motions measured from multi-epoch IR imaging from the Spitzer Space Telescope and Magellan Observatory and positions in CMDs measured with Gaia, 2MASS, VISTA VHS, WISE, Spitzer, and Magellan.
2. We have obtained optical and IR spectra of 365 candidate members of the populations near the Corona Australis cloud, which have been used to measure spectral types and diagnostics of youth. We also have compiled all objects in our survey field that have evidence of youth and that are not rejected as non-members by available measurements of proper motions and parallaxes. The resulting catalog contains 393 adopted members (39 at  $>M6$ ), 293 (36) of which are spectroscopically classified for the first time in this work.
3. Previous measurements of radial velocities are available for 82 of the adopted members. For the 72 stars that also have proper motions and parallaxes from Gaia EDR3, we have calculated  $UVW$  space velocities. Among the 55 stars with measured velocities and accurate and reliable astrometry ( $\sigma_\pi < 0.5$  mas,  $\text{RUWE} < 1.6$ ),  $W$  is correlated with the spatial position in  $Z$ , which suggests the presence of expansion along that dimension. Only a small number of the highly reddened stars ( $A_J > 1$ ) within the Corona Australis cloud have measurements of  $UVW$ , but those measurements fall within the range of velocities exhibited by the less obscured members. To expand the comparison of stars with low and high extinction to include those lacking radial velocity measurements, we have also considered their proper motion offsets and parallaxes. In those parameters, as with  $UVW$ , the embedded stars fall within the range of values for the less obscured members.
4. We have estimated the relative ages of low-mass stars (K5–M5) in Corona Australis using their offsets in  $M_K$  from the median sequence for Upper Sco in the H-R diagram. We calculated the medians of those offsets in three samples of members: stars near the cloud ( $b < -17.3^\circ$ ) with  $A_J > 1$

(concentrated in the Coronet Cluster), stars near the cloud ( $b < -17.3^\circ$ ) with  $A_J \leq 1$ , and stars farther from the cloud ( $b \geq -17.3^\circ$ ). Those median offsets have been converted to ages assuming an age of 10 Myr for Upper Sco and the luminosity evolution predicted by evolutionary models (Baraffe et al. 2015; Feiden 2016). We find that the near-cloud  $A_J > 1$  stars exhibit a significantly younger median age ( $\sim 1\text{--}2$  Myr) than the less obscured near-cloud stars ( $\sim 12$  Myr) and the off-cloud stars ( $\sim 15$  Myr). The second sample may appear slightly younger than the third one because of contamination from members of the younger population that have  $A_J < 1$ . Therefore, we propose that Corona Australis contains two populations, a younger one that is partially embedded in the cloud (the Coronet Cluster) and an older one that surrounds and extends beyond the cloud (Upper Corona Australis, Gagné et al. 2018).

5. The Coronet Cluster and Upper Corona Australis resemble Ophiuchus and Upper Sco in terms of their relative numbers of stars, spatial distributions, kinematics, and ages. In each region, 1) a population with an age of a few Myr is partially embedded within a molecular cloud and a population with an age of  $\gtrsim 10$  Myr surrounds the cloud and extends across a much larger area; 2) the cloud and its younger population are located near the edge of the older population; 3) the older population is substantially richer; and 4) the older population spans a wider range of kinematics that largely encompasses the narrower range of kinematics of the younger population.
6. Galli et al. (2020) identified candidate members of Corona Australis using data from Gaia DR2. Among those stars, they reported the presence of two populations – near the cloud and far from the cloud – that are distinct from each other in terms of proper motions. However, we find that the difference in proper motions is a reflection of the projection effects that arise for stars distributed across an extended area of sky. Instead, as mentioned previously, we find that the near-cloud and off-cloud stars have similar kinematics in terms of space velocities and proper motion offsets (which correct for projection effects).
7. We have used IR CMDs to characterize the completeness limits of our census of Corona Australis for the areas imaged by Spitzer and Magellan and the full survey field, arriving at limits that range from  $\sim 0.015\text{--}0.1 M_\odot$  for the levels of extinction encompassing most known members. We have constructed histograms of spectral type for extinction-limited samples of members within multiple fields, each of which exhibits a peak at M5 ( $\sim 0.15 M_\odot$ ), indicating that the IMF in Corona Australis has a similar characteristic mass as other nearby star-forming regions.
8. We have compiled mid-IR photometry from WISE and Spitzer for the adopted members of Corona Australis and we have used those data to search



for IR excesses from circumstellar disks. Excesses are detected for 122 stars, a third of which are reported for the first time in this work. The sizes of the excesses have been used to classify the evolutionary stages of the disks. The relative disk fractions among the three samples defined for the age analysis are consistent with the relative ages derived for those samples. The same is true for the disk fractions and ages of Upper Corona Australis ( $\sim 15$  Myr) relative to those in Upper Sco and UCL/LCC ( $\sim 10$  and  $20$  Myr).

K.L. acknowledges support from NASA grant 80NSSC18K0444 for portions of this work. We thank Katelyn Allers for providing the modified version of Spextool for use with ARCoIRIS data. The IRTF is operated by the University of Hawaii under contract 80HQTR19D0030 with NASA. The data at CTIO were obtained through programs 2016A-0157 and 2021A-0006 at NOIRLab. CTIO and NOIRLab are operated by the Association of Universities for Research in Astronomy under a cooperative agreement with the NSF. The Gemini data were obtained through programs GS-2008B-Q-12 (2008B-0185) and GS-2016A-Q-32 (2016A-0139). Gemini Observatory is operated by AURA under a cooperative agreement with the NSF on behalf of the Gemini partnership: the

NSF (United States), the NRC (Canada), CONICYT (Chile), Ministério da Ciência, Tecnologia e Inovação (Brazil), Ministerio de Ciencia, Tecnología e Innovación Productiva (Argentina), and Korea Astronomy and Space Science Institute (Republic of Korea). This work used data from the European Space Agency (ESA) mission Gaia (<https://www.cosmos.esa.int/gaia>), processed by the Gaia Data Processing and Analysis Consortium (DPAC, <https://www.cosmos.esa.int/web/gaia/dpac/consortium>). Funding for the DPAC has been provided by national institutions, in particular the institutions participating in the Gaia Multilateral Agreement. This work used data from the Spitzer Space Telescope and the NASA/IPAC Infrared Science Archive, operated by JPL under contract with NASA, and the VizieR catalog access tool and the SIMBAD database, both operated at CDS, Strasbourg, France. WISE is a joint project of the University of California, Los Angeles, and the JPL/Caltech, funded by NASA. 2MASS is a joint project of the University of Massachusetts and the Infrared Processing and Analysis Center (IPAC) at Caltech, funded by NASA and the NSF. The Center for Exoplanets and Habitable Worlds is supported by the Pennsylvania State University, the Eberly College of Science, and the Pennsylvania Space Grant Consortium.

*Facilities:* Blanco (COSMOS, ARCoIRIS), Gemini:South (Flamingos-2), IRTF (SpeX), Spitzer (IRAC, MIPS), WISE, Gaia, Magellan:Baade (FourStar, FIRE).

## REFERENCES

- Bailer-Jones, C. A. L., Rybizki, J., Fournesneau, M., Demleitner, M., & Andrae, R. 2021, *AJ*, 161, 147
- Baraffe, I., Chabrier, G., Allard, F., & Hauschildt, P. H. 1998, *A&A*, 337, 403
- Baraffe, I., Homeier, D., Allard, F., & Chabrier, G. 2015, *A&A*, 577, A42
- Bell, C. P. M., Mamajek, E. E., & Naylor, T. 2015, *MNRAS*, 454, 593
- Bouy, H., Brandner, W., Martín, E. L., et al. 2004, *A&A*, 424, 213
- Brown, A. G. A., Arenou, F., van Leeuwen, F., Lindegren, L., & Luri, X. 1997, in *ESA Special Publication*, Vol. 402, *Hipparcos - Venice '97*, ed. R. M. Bonnet, E. Høg, P. L. Bernacca, L. Emiliani, A. Blaauw, C. Turon, J. Kovalevsky, L. Lindegren, H. Hassan, M. Bouffard, B. Strim, D. Heger, M. A. C. Perryman, & L. Woltjer, 63–68
- Burrows, A., Marley, M., Hubbard, W. B., et al. 1997, *ApJ*, 491, 856
- Byers, S., & Raftery, A. E. 1998, *Journal of the American Statistical Association*, 93, 577
- Carmona, A., van den Ancker, M. E., & Henning, T. 2007, *A&A*, 464, 687
- Cazzoletti, P., Manara, C. F., Baobab Liu, H., et al. 2019, *A&A*, 626, A11
- Chabrier, G., Baraffe, I., Allard, F., & Hauschildt, P. 2000, *ApJ*, 542, 464
- Currie, T., & Sicilia-Aguilar, A. 2011, *ApJ*, 732, 24
- Cushing, M. C., Rayner, J. T., & Vacca, W. D. 2005, *ApJ*, 623, 1115
- Cushing, M. C., Vacca, W. D., & Rayner, J. T. 2004, *PASP*, 116, 362
- Cutri, R. M., Wright, E. L., Conrow, T., et al. 2012, *Explanatory Supplement to the WISE All-Sky Data Release Products*, Explanatory Supplement to the WISE All-Sky Data Release Products, ,
- Dobashi, K., Marshall, D. J., Shimoikura, T., & Bernard, J.-P. 2013, *PASJ*, 65, 31
- Dressler, A., Bigelow, B., Hare, T., et al. 2011, *PASP*, 123, 288
- Eikenberry, S. S., Elston, R., Raines, S. N., et al. 2004, in *Society of Photo-Optical Instrumentation Engineers (SPIE) Conference Series*, Vol. 5492, *Ground-based Instrumentation for Astronomy*, ed. A. F. M. Moorwood & M. Iye, 1196–1207
- Espallat, C., Ingleby, L., Hernández, J., et al. 2012, *ApJ*, 747, 103
- Esplin, T. L., & Luhman, K. L. 2016, *AJ*, 151, 9
- . 2019, *AJ*, 158, 54
- . 2020, *AJ*, 159, 282
- Esplin, T. L., Luhman, K. L., Faherty, J. K., Mamajek, E. E., & Bochanski, J. J. 2017, *AJ*, 154, 46
- Esplin, T. L., Luhman, K. L., & Mamajek, E. E. 2014, *ApJ*, 784, 126
- Esplin, T. L., Luhman, K. L., Miller, E. B., & Mamajek, E. E. 2018, *AJ*, 156, 75
- Fazio, G. G., Hora, J. L., Allen, L. E., et al. 2004, *ApJS*, 154, 10
- Feiden, G. A. 2016, *A&A*, 593, A99
- Fernández, M., & Comerón, F. 2001, *A&A*, 380, 264
- Filippazzo, J. C., Rice, E. L., Faherty, J., et al. 2015, *ApJ*, 810, 158
- Forbrich, J., & Preibisch, T. 2007, *A&A*, 475, 959
- Forbrich, J., Preibisch, T., & Menten, K. M. 2006, *A&A*, 446, 155
- Gagné, J., Mamajek, E. E., Malo, L., et al. 2018, *ApJ*, 856, 23
- Gaia Collaboration, Brown, A. G. A., Vallenari, A., et al. 2016, *A&A*, 595, A2
- . 2018, *A&A*, 616, A1
- . 2021, *A&A*, 649, A1
- Galli, P. A. B., Bouy, H., Olivares, J., et al. 2020, *A&A*, 634, A98
- Glass, I. S., & Penston, M. V. 1975, *MNRAS*, 172, 227
- Gray, R. O., Corbally, C. J., Garrison, R. F., et al. 2006, *AJ*, 132, 161
- Gutermuth, R. A., Megeath, S. T., Myers, P. C., et al. 2009, *ApJS*, 184, 18
- Hennig, C., & Hausdorf, B. 2019, *prabclus: Functions for Clustering and Testing of Presence-Absence, Abundance and Multilocus Genetic Data*, *r* package version 2.3-1
- Henry, T. J., Kirkpatrick, J. D., & Simons, D. A. 1994, *AJ*, 108, 1437
- Herbig, G. H., & Bell, K. R. 1988, *Third Catalog of Emission-Line Stars of the Orion Population : 3 : 1988*

- Herczeg, G. J., & Hillenbrand, L. A. 2014, *ApJ*, 786, 97
- Hernández, J., Hartmann, L., Megeath, T., et al. 2007, *ApJ*, 662, 1067
- Hook, I. M., Jørgensen, I., Allington-Smith, J. R., et al. 2004, *PASP*, 116, 425
- Houk, N. 1982, *Michigan Catalogue of Two-dimensional Spectral Types for the HD stars. Volume.3. Declinations -40 to -26.*
- Indebetouw, R., Mathis, J. S., Babler, B. L., et al. 2005, *ApJ*, 619, 931
- Johnson, D. R. H., & Soderblom, D. R. 1987, *AJ*, 93, 864
- Jönsson, H., Holtzman, J. A., Allende Prieto, C., et al. 2020, *AJ*, 160, 120
- Joy, A. H. 1954, *PASP*, 66, 5
- Kenyon, S. J., & Bromley, B. C. 2005, *AJ*, 130, 269
- Kirkpatrick, J. D., Henry, T. J., & Irwin, M. J. 1997, *AJ*, 113, 1421
- Kirkpatrick, J. D., Henry, T. J., & McCarthy, Donald W., J. 1991, *ApJS*, 77, 417
- Lindgren, L. 2018, *gAIA-C3-TN-LU-LL-124*
- López Martí, B., Eislöf, J., & Mundt, R. 2005, *A&A*, 444, 175
- Lucas, P. W., Roche, P. F., Allard, F., & Hauschildt, P. H. 2001, *MNRAS*, 326, 695
- Luhman, K. L. 1999, *ApJ*, 525, 466
- . 2018, *AJ*, 156, 271
- . 2021a, *AJ*, submitted
- . 2021b, *AJ*, in press
- Luhman, K. L., Allen, P. R., Espaillat, C., Hartmann, L., & Calvet, N. 2010, *ApJS*, 186, 111
- Luhman, K. L., & Esplin, T. L. 2020, *AJ*, 160, 44
- Luhman, K. L., Esplin, T. L., & Loutrel, N. P. 2016, *ApJ*, 827, 52
- Luhman, K. L., Liebert, J., & Rieke, G. H. 1997, *ApJ*, 489, L165
- Luhman, K. L., & Mamajek, E. E. 2012, *ApJ*, 758, 31
- Luhman, K. L., Mamajek, E. E., Shukla, S. J., & Loutrel, N. P. 2017, *AJ*, 153, 46
- Luhman, K. L., Rieke, G. H., Lada, C. J., & Lada, E. A. 1998, *ApJ*, 508, 347
- Makovoz, D., & Marleau, F. R. 2005, *PASP*, 117, 1113
- Mamajek, E. E. 2009, in *American Institute of Physics Conference Series*, Vol. 1158, American Institute of Physics
- Conference Series, ed. T. Usuda, M. Tamura, & M. Ishii, 3–10
- Marraco, H. G., & Rydgren, A. E. 1981, *AJ*, 86, 62
- Martin, E. L., Rebolo, R., & Zapatero-Osorio, M. R. 1996, *ApJ*, 469, 706
- Martini, P., Stoll, R., Derwent, M. A., et al. 2011, *PASP*, 123, 187
- McMahon, R. G., Banerji, M., Gonzalez, E., et al. 2013, *The Messenger*, 154, 35
- Meyer, M. R., & Wilking, B. A. 2003, in *American Astronomical Society Meeting Abstracts*, Vol. 202, American Astronomical Society Meeting Abstracts #202, 28.06
- Meyer, M. R., & Wilking, B. A. 2009, *PASP*, 121, 350
- Neuhäuser, R., & Forbrich, J. 2008, *The Corona Australis Star Forming Region*, ed. B. Reipurth, Vol. 5, 735
- Neuhäuser, R., Walter, F. M., Covino, E., et al. 2000, *A&AS*, 146, 323
- Nisini, B., Antonucci, S., Giannini, T., & Lorenzetti, D. 2005, *A&A*, 429, 543
- Nutter, D. J., Ward-Thompson, D., & André, P. 2005, *MNRAS*, 357, 975
- Olofsson, G., Hultgren, M., Kaas, A. A., et al. 1999, *A&A*, 350, 883
- Patten, B. M. 1998, in *Astronomical Society of the Pacific Conference Series*, Vol. 154, Cool Stars, Stellar Systems, and the Sun, ed. R. A. Donahue & J. A. Bookbinder, 1755
- Pecaut, M. J., & Mamajek, E. E. 2016, *MNRAS*, 461, 794
- Pecaut, M. J., Mamajek, E. E., & Bubar, E. J. 2012, *ApJ*, 746, 154
- Perryman, M. A. C., de Boer, K. S., Gilmore, G., et al. 2001, *A&A*, 369, 339
- Persson, S. E., Murphy, D. C., Smee, S., et al. 2013, *PASP*, 125, 654
- Peterson, D. E., Caratti o Garatti, A., Bourke, T. L., et al. 2011, *ApJS*, 194, 43
- Prato, L., Greene, T. P., & Simon, M. 2003, *ApJ*, 584, 853
- R Core Team. 2017, *R: A Language and Environment for Statistical Computing*, R Foundation for Statistical Computing, Vienna, Austria
- Rayner, J. T., Cushing, M. C., & Vacca, W. D. 2009, *ApJS*, 185, 289
- Rayner, J. T., Toomey, D. W., Onaka, P. M., et al. 2003, *PASP*, 115, 362
- Reipurth, B., & Zinnecker, H. 1993, *A&A*, 278, 81
- Rieke, G. H., Young, E. T., Engelbracht, C. W., et al. 2004, *ApJS*, 154, 25
- Rieke, G. H., Su, K. Y. L., Stansberry, J. A., et al. 2005, *ApJ*, 620, 1010
- Romero, G. A., Schreiber, M. R., Cieza, L. A., et al. 2012, *ApJ*, 749, 79
- Schlafly, E. F., Meisner, A. M., Stutz, A. M., et al. 2016, *ApJ*, 821, 78
- Schlawin, E., Herter, T. L., Henderson, C., et al. 2014, in *Society of Photo-Optical Instrumentation Engineers (SPIE) Conference Series*, Vol. 9147, Ground-based and Airborne Instrumentation for Astronomy V, ed. S. K. Ramsay, I. S. McLean, & H. Takami, 91472H
- Scrucca, L., Pop, M., Murphy, T. B., & Raftery, A. E. 2016, *The R Journal*, 8, 205
- Sicilia-Aguilar, A., Henning, T., Juhász, A., et al. 2008, *ApJ*, 687, 1145
- Sicilia-Aguilar, A., Henning, T., Kainulainen, J., & Roccatagliata, V. 2011, *ApJ*, 736, 137
- Simcoe, R. A., Burgasser, A. J., Schechter, P. L., et al. 2013, *PASP*, 125, 270
- Skrutskie, M. F., Cutri, R. M., Stiening, R., et al. 2006, *AJ*, 131, 1163
- Suárez, O., García-Lario, P., Manchado, A., et al. 2006, *A&A*, 458, 173
- Taylor, K. N. R., & Storey, J. W. V. 1984, *MNRAS*, 209, 5P
- Torres, C. A. O., Quast, G. R., da Silva, L., et al. 2006, *A&A*, 460, 695
- Vacca, W. D., Cushing, M. C., & Rayner, J. T. 2003, *PASP*, 115, 389
- Vieira, S. L. A., Corradi, W. J. B., Alencar, S. H. P., et al. 2003, *AJ*, 126, 2971
- Walter, F. M., Vrba, F. J., Wolk, S. J., Mathieu, R. D., & Neuhäuser, R. 1997, *AJ*, 114, 1544
- Werner, M. W., Roellig, T. L., Low, F. J., et al. 2004, *ApJS*, 154, 1
- Whitworth, A., Bate, M. R., Nordlund, Å., Reipurth, B., & Zinnecker, H. 2007, in *Protostars and Planets V*, ed. B. Reipurth, D. Jewitt, & K. Keil, 459
- Wilking, B. A., McCaughrean, M. J., Burton, M. G., et al. 1997, *AJ*, 114, 2029
- Wright, E. L., Eisenhardt, P. R. M., Mainzer, A. K., et al. 2010, *AJ*, 140, 1868

TABLE 1  
ADOPTED MEMBERS OF CORONA AUSTRALIS

Column Label	Description
2MASS	2MASS Point Source Catalog source name
WISE	WISE source name <sup>a</sup>
Gaia	Gaia EDR3 source name
GP75 R CrA	Designation from Glass & Penston (1975)
TS84	Designation from Taylor & Storey (1984)
HBC	Designation from Herbig & Bell (1988)
WMB97	Designation from Wilking et al. (1997)
CrAPMS	Designation from Walter et al. (1997)
P98c	Designation from Patten (1998)
ISO-CrA	Designation from Olofsson et al. (1999)
RX	Designation from Neuhäuser et al. (2000)
LEM2005b CrA	Designation from López Martí et al. (2005)
FP2007	Designation from Forbrich & Preibisch (2007)
SHJ2008	Designation from Sicilia-Aguilar et al. (2008)
GMM2009	Designation from Gutermuth et al. (2009)
PCB2011 CrA	Designation from Peterson et al. (2011)
OName	Other common identifier
RAdeg	Right Ascension (ICRS)
DEdeg	Declination (ICRS)
Ref-Pos	Reference for RAdeg and DEdeg <sup>b</sup>
SpType	Spectral type
r.SpType	Reference for SpType <sup>c</sup>
Adopt	Adopted spectral type
GaiapmRA	Proper motion in right ascension from Gaia EDR3
e.GaiapmRA	Error in GaiapmRA
GaiapmDec	Proper motion in declination from Gaia EDR3
e.GaiapmDec	Error in GaiapmDec
plx	Parallax from Gaia EDR3
e.plx	Error in plx
RUWE	Re-normalized unit weight error from Gaia EDR3
kin	Satisfies Gaia kinematic criteria?
r.med_geo	Median of the geometric distance posterior from Bailer-Jones et al. (2021)
r.lo_geo	16th percentile of the geometric distance posterior from Bailer-Jones et al. (2021)
r.hi_geo	84th percentile of the geometric distance posterior from Bailer-Jones et al. (2021)
IRpmRA	Proper motion in right ascension from IR images
e.IRpmRA	Error in IRpmRA
IRpmDec	Proper motion in declination from IR images
e.IRpmDec	Error in IRpmDec
RVel	Radial velocity
e.RVel	Error in RVel
r.RVel	Radial velocity reference <sup>d</sup>
U	$U$ component of space velocity
e.U	Error in $U$
V	$V$ component of space velocity
e.V	Error in $V$
W	$W$ component of space velocity
e.W	Error in $W$
Gmag	$G$ magnitude from Gaia EDR3
e.Gmag	Error in Gmag
GBPmag	$G_{BP}$ magnitude from Gaia EDR3
e.GBPmag	Error in GBPmag
GRPmag	$G_{RP}$ magnitude from Gaia EDR3
e.GRPmag	Error in GRPmag
Jmag	$J$ magnitude
e.Jmag	Error in Jmag
r.Jmag	Reference for Jmag <sup>e</sup>
Hmag	$H$ magnitude
e.Hmag	Error in Hmag
r.Hmag	Reference for Hmag <sup>e</sup>
Kmag	$K_s$ or $K$ magnitude
e.Kmag	Error in Kmag
r.Kmag	Reference for Kmag <sup>e</sup>
3.6mag	Spitzer [3.6] magnitude
e.3.6mag	Error in 3.6mag
f.3.6mag	Flag on 3.6mag <sup>f</sup>
4.5mag	Spitzer [4.5] magnitude
e.4.5mag	Error in [4.5] magnitude
f.4.5mag	Flag on 4.5mag <sup>f</sup>
5.8mag	Spitzer [5.8] magnitude
e.5.8mag	Error in 5.8mag
f.5.8mag	Flag on 5.8mag <sup>f</sup>
8.0mag	Spitzer [8.0] magnitude
e.8.0mag	Error in 8.0mag
f.8.0mag	Flag on 8.0mag <sup>f</sup>

TABLE 1 — *Continued*

Column Label	Description
24mag	Spitzer [24] magnitude
e_24mag	Error in 24mag
f_24mag	Flag on 24mag <sup>f</sup>
W1mag	WISE W1 magnitude
e_W1mag	Error in W1mag
f_W1mag	Flag on W1mag <sup>f</sup>
W2mag	WISE W2 magnitude
e_W2mag	Error in W2mag
f_W2mag	Flag on W2mag <sup>f</sup>
W3mag	WISE W3 magnitude
e_W3mag	Error in W3mag
f_W3mag	Flag on W3mag <sup>f</sup>
W4mag	WISE W4 magnitude
e_W4mag	Error in W4mag
f_W4mag	Flag on W4mag <sup>f</sup>
Exc4.5	Excess present in [4.5]?
Exc8.0	Excess present in [8.0]?
Exc24	Excess present in [24]?
ExcW2	Excess present in W2?
ExcW3	Excess present in W3?
ExcW4	Excess present in W4?
DiskType	Disk Type
Ak	Extinction in K
f_Ak	Method for estimating Ak <sup>g</sup>

NOTE. — This table is available in its entirety in a machine-readable form.

<sup>a</sup> Coordinate-based identifications from the AllWISE Source Catalog when available. Otherwise, identifications are from the AllWISE Reject Table or the WISE All-Sky Catalog.

<sup>b</sup> 2MASS = 2MASS Point Source Catalog; Gaia = Gaia EDR3 (Epoch 2016.0); IRAC = derived from IRAC images in this work.

<sup>c</sup> 1 = This Work; 2 = Torres et al. (2006); 3 = Houk (1982); 4 = Neuhäuser et al. (2000); 5 = Cazzoletti et al. (2019); 6 = Walter et al. (1997); 7 = Patten (1998); 8 = Bouy et al. (2004); 9 = Herbig & Bell (1988); 10 = Romero et al. (2012); 11 = Sicilia-Aguilar et al. (2011); 12 = López Martí et al. (2005); 13 = Sicilia-Aguilar et al. (2008); 14 = Carmona et al. (2007); 15 = Prato et al. (2003); 16 = Meyer & Wilking (2009); 17 = Reipurth & Zinnecker (1993); 18 = Fernández & Comerón (2001); 19 = Marraco & Rydgren (1981); 20 = Vieira et al. (2003); 21 = Nisini et al. (2005); 22 = Meyer & Wilking (2003); 23 = Gray et al. (2006); 24 = Herczeg & Hillenbrand (2014); 25 = Joy (1954); 26 = Suárez et al. (2006).

<sup>d</sup> 1 = Gaia DR2; 2 = Jönsson et al. (2020); 3 = Torres et al. (2006).

<sup>e</sup> 2MASS = 2MASS Point Source Catalog; Fs18 = our FourStar photometry; VHS = VHS Data Release 6.

<sup>f</sup> nodet = non-detection; sat = saturated; out = outside of the camera’s field of view; bl = photometry may be affected by blending with a nearby star; bin = includes an unresolved binary companion; err = W2 magnitudes brighter than 6 mag are erroneous; unres = too close to a brighter star to be detected; ext = photometry is known or suspected to be contaminated by extended emission (no data given when extended emission dominates); false = detection from WISE catalog appears false or unreliable based on visual inspection.

<sup>g</sup> J-H and H-K = derived from these colors assuming photospheric near-IR colors (Luhman & Esplin 2020); IR spec = derived from an IR spectrum.

TABLE 2  
IRAC OBSERVATIONS OF CORONA AUSTRALIS

AOR	PID	PI	epoch
3650816	6	G. Fazio	2004.3
17672960	30784	G. Fazio	2006.7
17673472	30784	G. Fazio	2006.7
27041280	30574	L. Allen	2008.4
47018240	90071	A. Kraus	2012.9
47018496	90071	A. Kraus	2012.9
47018752	90071	A. Kraus	2012.9
47019008	90071	A. Kraus	2012.9
47019264	90071	A. Kraus	2012.9
47019520	90071	A. Kraus	2012.9
47019776	90071	A. Kraus	2012.9
47020032	90071	A. Kraus	2012.9
47020288	90071	A. Kraus	2012.9
47020544	90071	A. Kraus	2012.9

TABLE 3  
OBSERVING LOG

Telescope/Instrument	Disperser/Aperture	Wavelengths/Resolution	Targets
IRTF/SpeX	prism/0'8 slit	0.8–2.5 $\mu\text{m}$ /R=150	164
4m Blanco CTIO/COSMOS	red VPH/0'9 slit	0.55–0.95 $\mu\text{m}$ /3 Å	148
4m Blanco CTIO/ARCoIRIS	110.5 l mm <sup>-1</sup> + prism/1'1 slit	0.8–2.47 $\mu\text{m}$ /R=3500	53
Gemini South/GMOS	R400/0'75 slit	0.6–1 $\mu\text{m}$ /6 Å	1
Gemini South/FLAMINGOS-2	HK Grism/0'72 slit	1.10–2.65 $\mu\text{m}$ /R=450	2
Magellan/FIRE	prism/0'8 slit	0.8–2.5 $\mu\text{m}$ /R=100	23

TABLE 4  
SPECTROSCOPIC DATA FOR CANDIDATE MEMBERS OF CORONA AUSTRALIS

Source Name <sup>a</sup>	Spectral Type	Instrument	Date	Young?	Satisfies Gaia Kinematic Criteria?	Adopted Member of RCrA?
2MASS J18204248-3701412	M5	SpeX	2021 May 11	Y	Y	Y
2MASS J18205562-3426455	M8	SpeX	2020 Aug 14	Y	...	N?
2MASS J18214722-3909565	M5.5	SpeX	2021 May 12	Y	Y	Y
2MASS J18215513-3718049	K7	COSMOS	2021 Jun 19	Y	Y	Y
2MASS J18222970-3434131	M5.5	COSMOS	2021 Jun 19	Y	Y	Y

NOTE. — This table is available in its entirety in a machine-readable form. A portion is shown is here for guidance regarding its form and content.

<sup>a</sup> Identifications are from the 2MASS Point Source Catalog when available. Otherwise, they are from Gaia EDR3 or VHS DR6.

TABLE 5  
GAIA CANDIDATES WITHOUT SPECTROSCOPY

Gaia EDR3	Right Ascension <sup>a</sup>	Declination <sup>a</sup>	<i>G</i>
Kinematic Candidates with RUWE<1.6			
4044760647651736064	275.630538	−33.457568	14.11
6733365816472640000	278.847121	−36.348380	19.72
6733973361050980352	279.801448	−34.870714	19.74
6729752954388414976	280.714523	−38.492150	19.15
6733635914059722752	281.078293	−35.640243	12.42
6729296107305930624	281.685646	−38.872435	19.79
6730249800505083392	282.358207	−37.277634	17.17
6732206067902438144	282.633911	−35.201108	18.17
6731205138658643584	285.707301	−36.773380	15.28
6756775415446336640	286.206810	−32.601102	16.91
Kinematic Candidates with RUWE>1.6			
6727177421432130560	277.322152	−37.763763	14.06
6735189150342584320	281.545001	−34.944044	16.16
Non-kinematic Candidate Companions			
6734638707323220992	278.809732	−34.718309	20.65
6730058107518665344	279.848667	−37.497411	19.51
6733690309836940672	280.231271	−35.371319	19.83
6733691134465880192	280.553312	−35.610333	20.52
6730364218421820928	280.760560	−37.461903	19.89
6730572335360428416	281.160780	−36.365688	20.37
6730228360027665536	281.821826	−37.567360	15.62
6731791659404134528	283.032778	−36.692146	13.93
6717001475652511488	283.738020	−39.854994	20.65
6731220085144465280	285.419170	−36.742231	14.68
6719180123582696192	285.799478	−37.150721	16.27

<sup>a</sup> From Gaia EDR3 (ICRS at Epoch 2016.0).

TABLE 6  
DISK FRACTIONS IN CORONA AUSTRALIS

Sample	<K6	K6–M3.5	M3.75–M5.75	M6–M8
$b \geq -17.3^\circ$ and $A_J \leq 1$	2/11=0.18 $^{+0.16}_{-0.06}$	9/68=0.13 $^{+0.05}_{-0.03}$	18/120=0.15 $^{+0.04}_{-0.03}$	10/39=0.25 $^{+0.08}_{-0.06}$

TABLE 6 — *Continued*

Sample	<K6	K6–M3.5	M3.75–M5.75	M6–M8
$b < -17.3^\circ$ and $A_J \leq 1$	1/6=0.17 $^{+0.23}_{-0.06}$	6/17=0.35 $^{+0.13}_{-0.09}$	12/34=0.35 $^{+0.09}_{-0.08}$	5/7=0.71 $^{+0.10}_{-0.20}$
$b < -17.3^\circ$ and $A_J > 1$	3/3=1.00 $^{+0.00}_{-0.37}$	7/9=0.77 $^{+0.08}_{-0.18}$	4/9=0.44 $^{+0.16}_{-0.14}$	1/3=0.33 $^{+0.28}_{-0.15}$

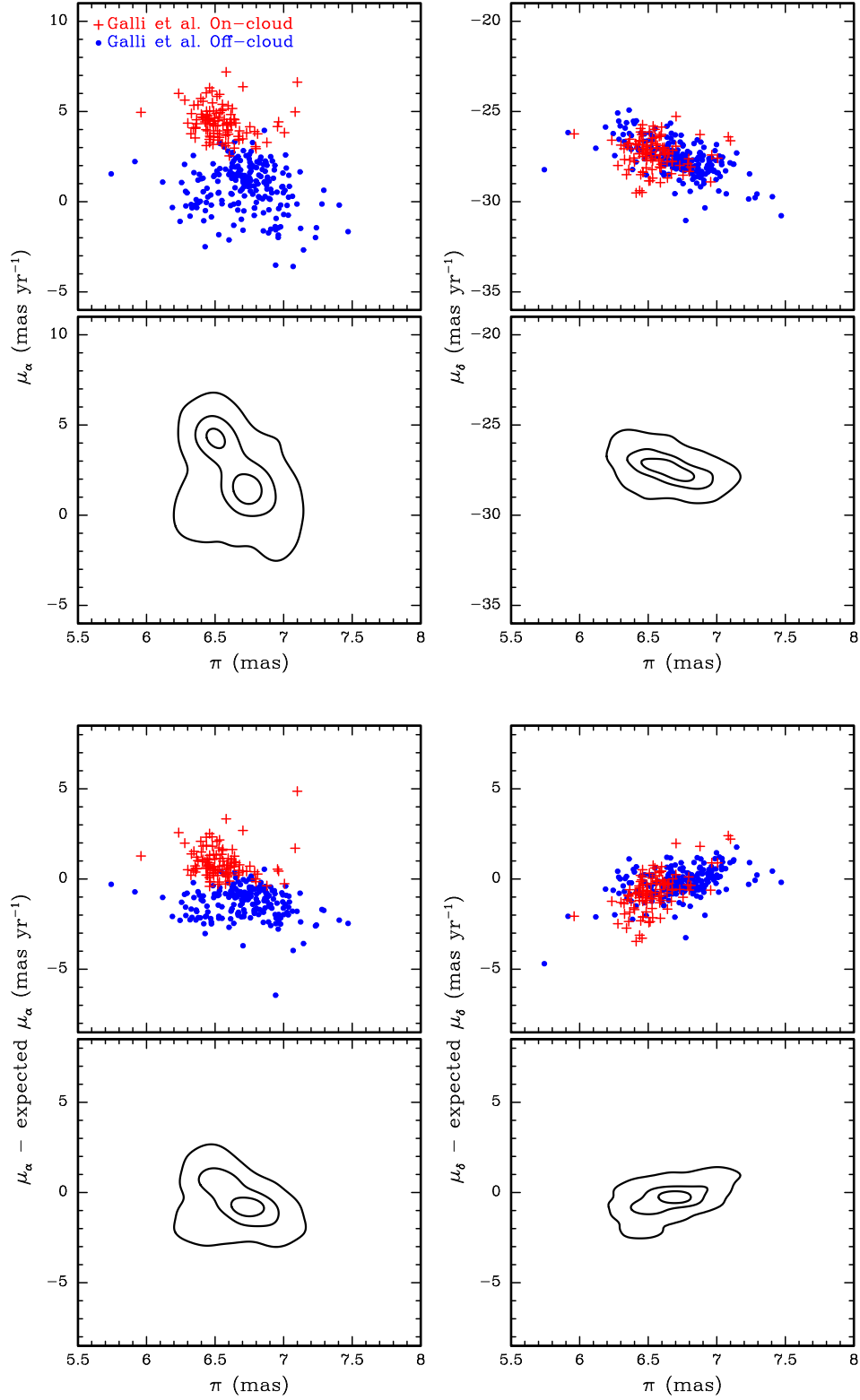


FIG. 1.— Proper motions (top two rows) and proper motion offsets (bottom two rows) versus parallax based on Gaia EDR3 for two samples of candidate members of Corona Australis from Galli et al. (2020). The offsets are computed relative to the proper motions expected for the positions and parallaxes assuming the median space velocity of known members. The contour levels are set at 10, 50, and 80% of the maximum densities. The bimodal nature of the candidates in  $\mu_\alpha$  is a reflection of projection effects, which are minimized in the proper motion offsets.

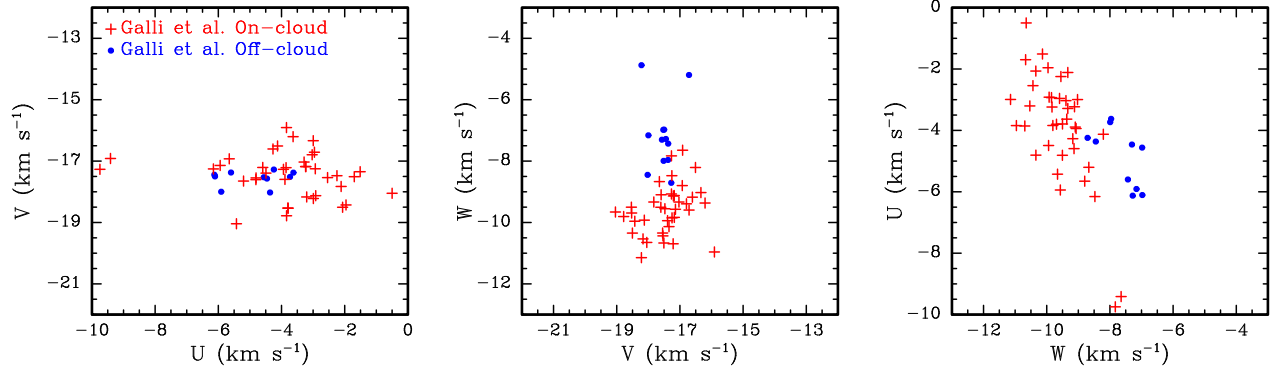


FIG. 2.— Space velocities for two samples of candidate members of Corona Australis from Galli et al. (2020) that have measurements of parallaxes and radial velocities.

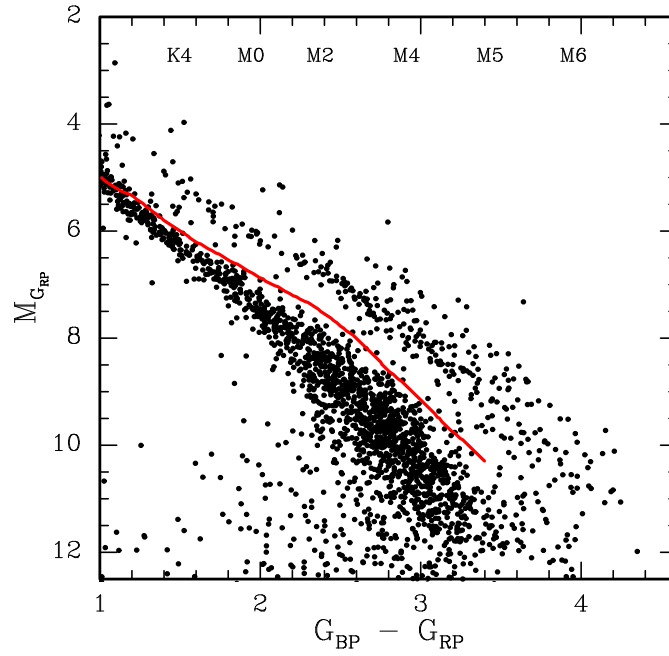


FIG. 3.—  $M_{G_{RP}}$  versus  $G_{BP} - G_{RP}$  for Gaia EDR3 sources near Corona Australis with  $5.5 < \pi < 8.5$  mas. The single star sequence of the Tuc-Hor association is indicated (45 Myr, Bell et al. 2015) (solid line). The spectral types that correspond to these colors for young stars are marked (Luhman 2021a).



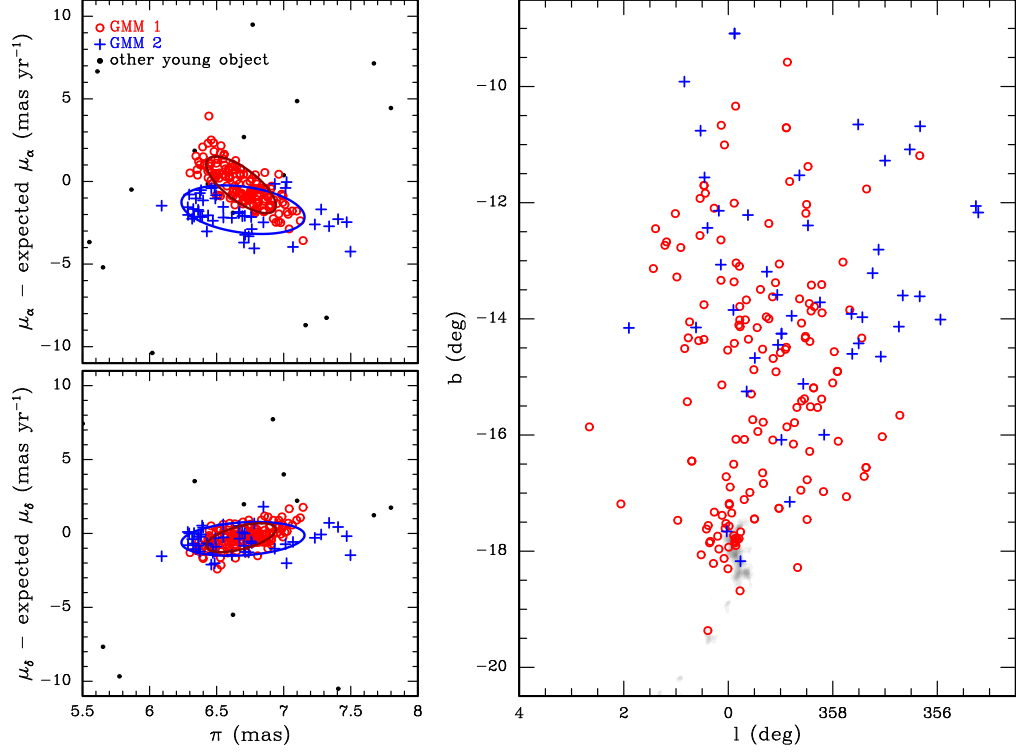


FIG. 4.— Proper motion offsets versus parallax for candidate young low-mass stars near Corona Australis from Figure 3 (left). We have applied a GMM to these data, which consists of two clustered components (red circles and blue pluses) and a noise population (black points). The  $2\sigma$  ellipses for the two model components are shown. The spatial distribution of the members of the components are plotted in the right panel. The large overlap of the two components suggests that they comprise a single non-gaussian population rather than two distinct populations. Extinction from the Corona Australis cloud is displayed in the diagram on the right (gray scale; Dobashi et al. 2013).

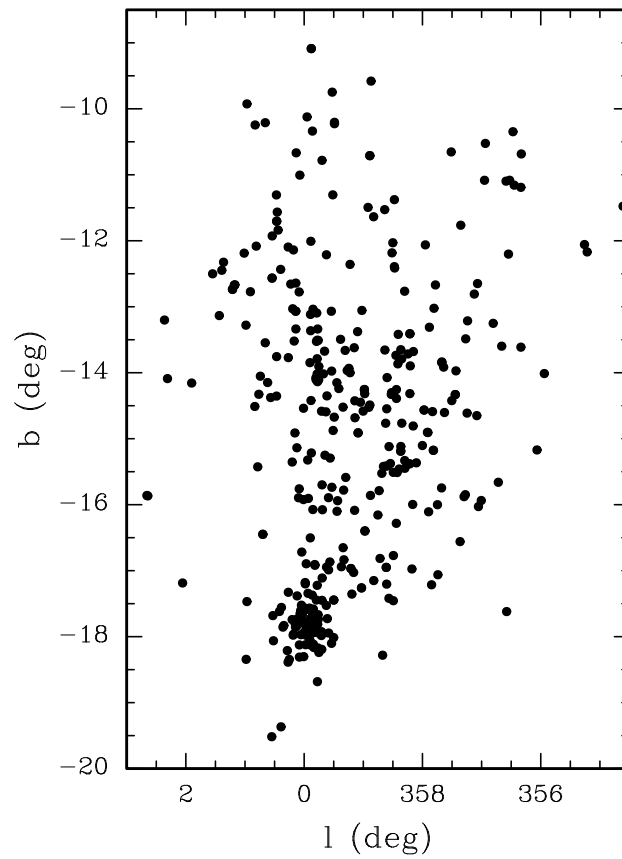


FIG. 5.— Spatial distribution of the adopted members of Corona Australis (Table 1).

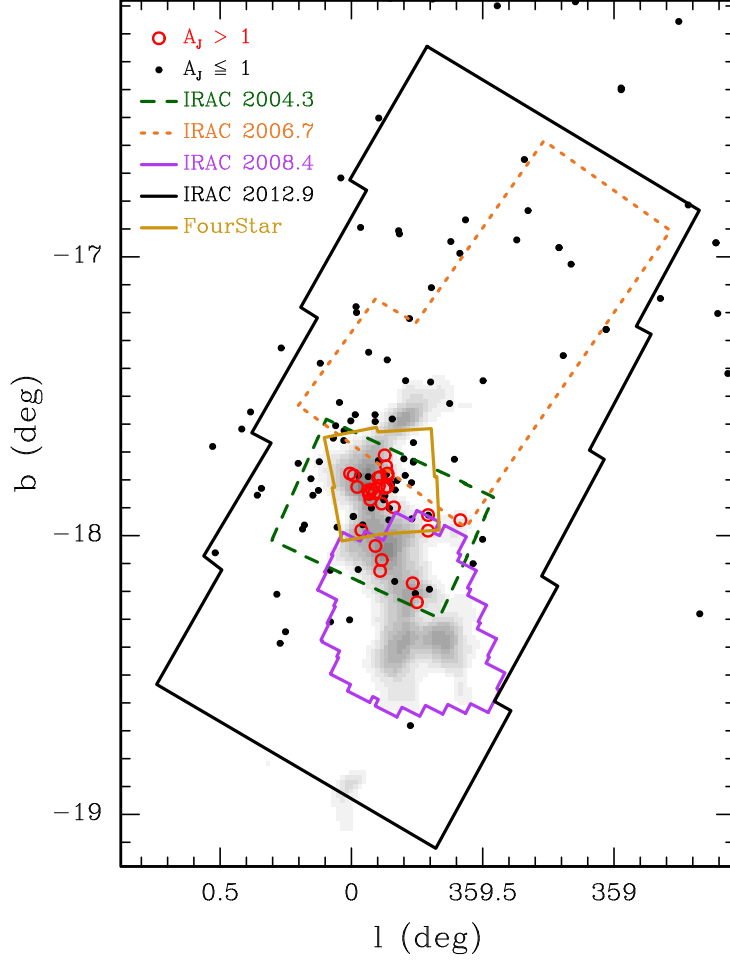


FIG. 6.— Map of the fields toward Corona Australis that have been imaged by IRAC on Spitzer (Table 2) and FourStar on Magellan. The known members are plotted with symbols based on their extinction. The Corona Australis cloud is represented by an extinction map (gray scale; Dobashi et al. 2013).

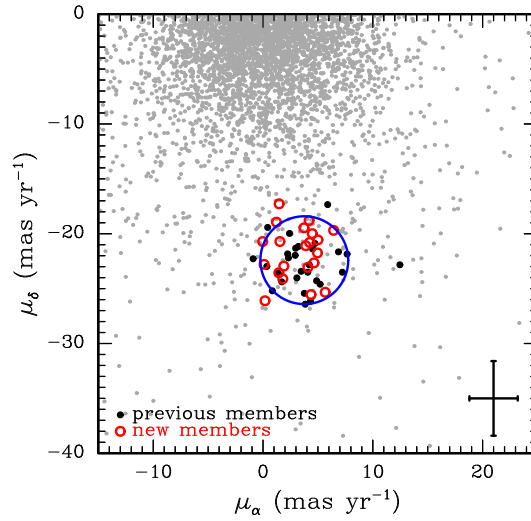


FIG. 7.— Relative proper motions based on multi-epoch imaging from IRAC and FourStar for Corona Australis, consisting of previously known members (black points), new members from our spectroscopic survey (red circles), and all other sources (gray points). The typical errors are indicated. Sources within  $1\sigma$  of the blue circle were selected as candidate members.

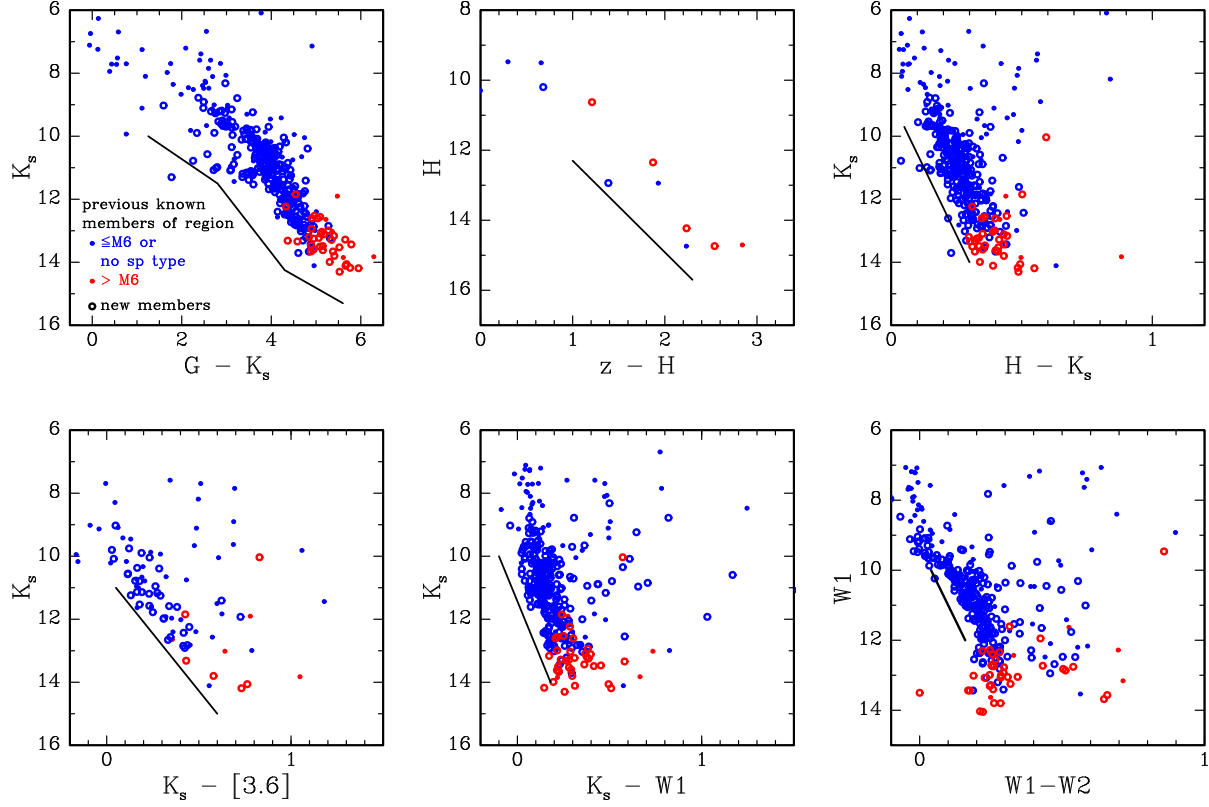


FIG. 8.— Extinction-corrected CMDs of the previously known members of Corona Australis (points) and new members from our spectroscopic survey (circles). We have selected candidate members based on positions above the solid boundaries.

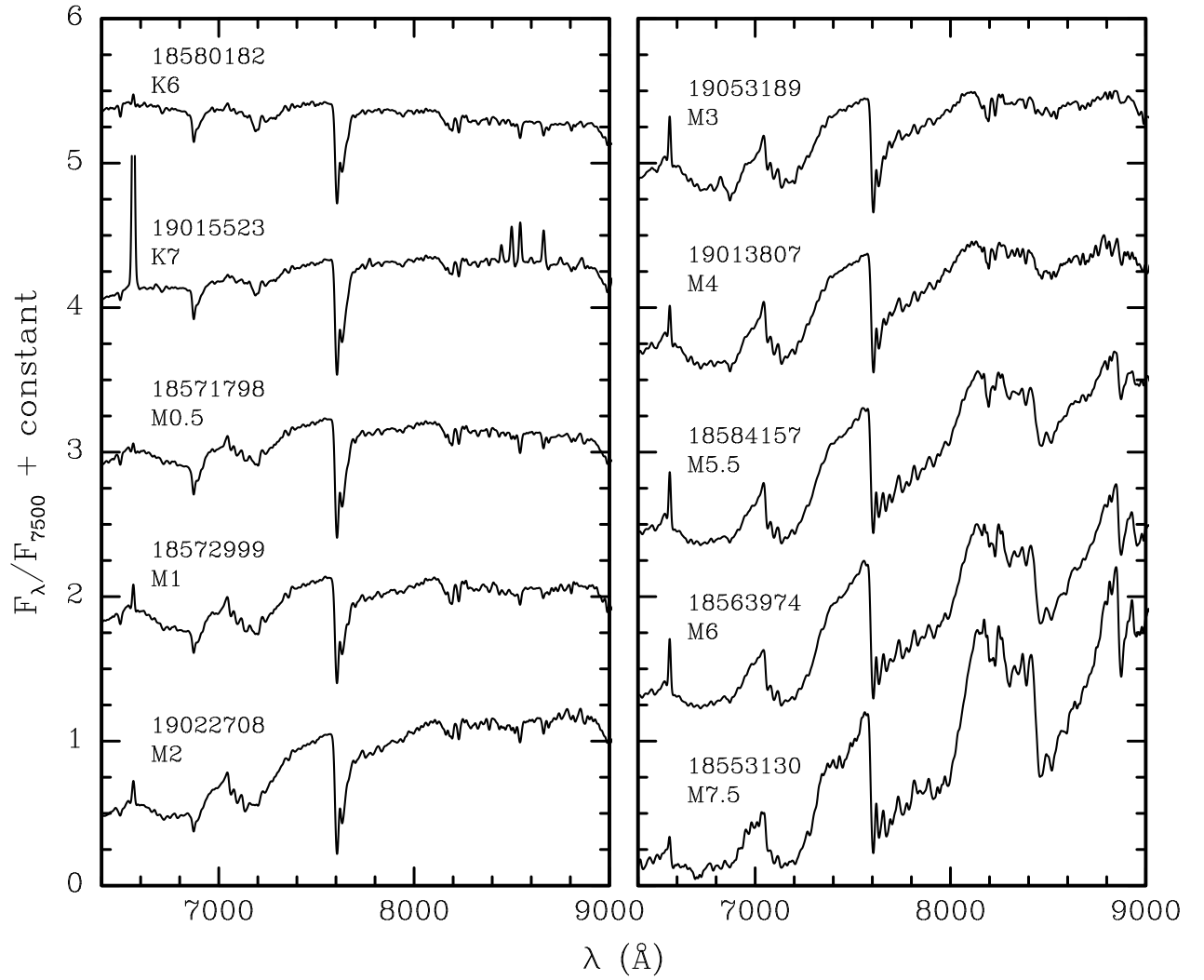


FIG. 9.— Examples of optical spectra of new members of Corona Australis (Table 4). The spectra have been smoothed to a resolution of 13 Å. The data used to create this figure are available.

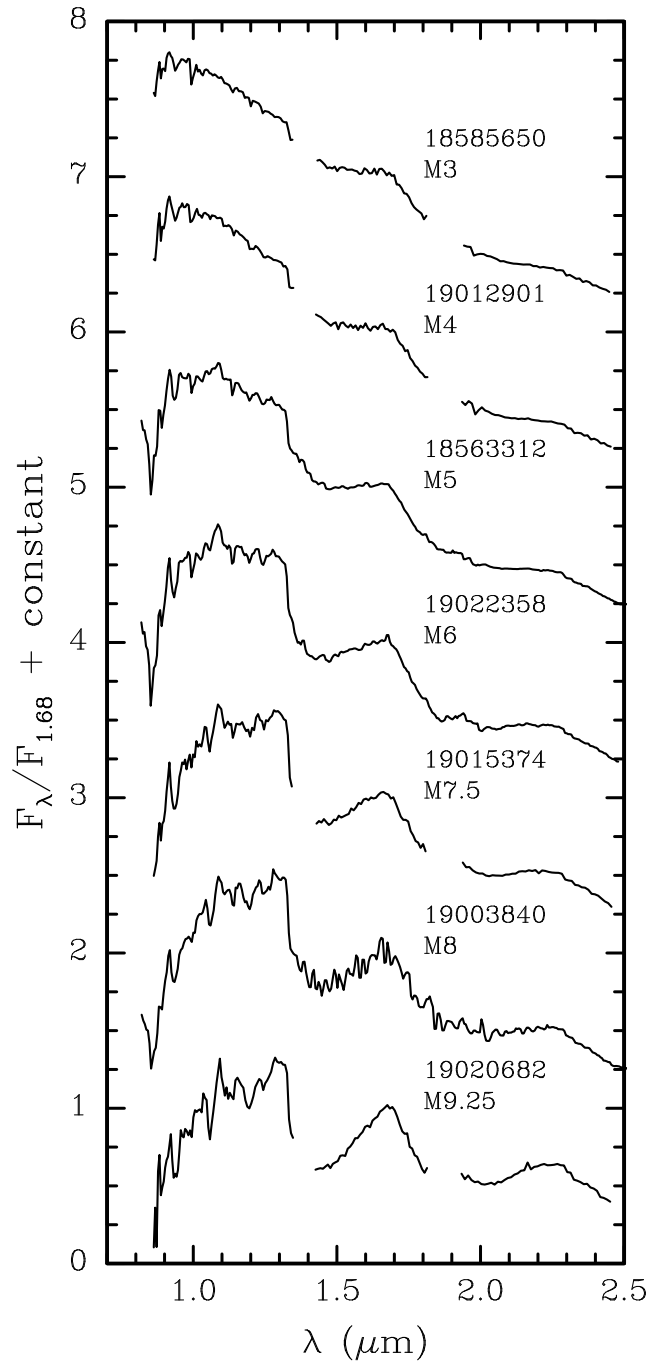


FIG. 10.— Examples of IR spectra of new members of Corona Australis (Table 4). The spectra have been dereddened to match the slopes of young standards from Luhman et al. (2017). The data used to create this figure are available.

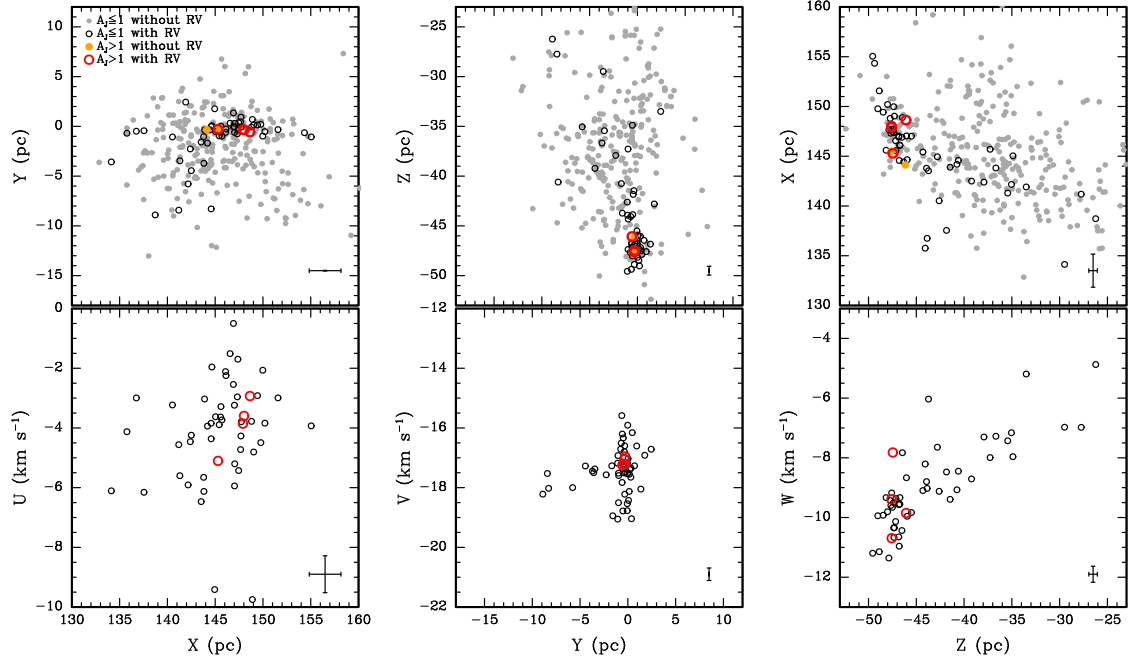


FIG. 11.— Top: Galactic Cartesian coordinates for members of Corona Australis with  $\sigma_\pi < 0.5$  and  $\text{RUWE} < 1.6$  (Table 1). Bottom: Stars that have radial velocity measurements are plotted in diagrams of  $U$ ,  $V$ , and  $W$  versus  $X$ ,  $Y$ , and  $Z$ , respectively. The average errors are indicated.

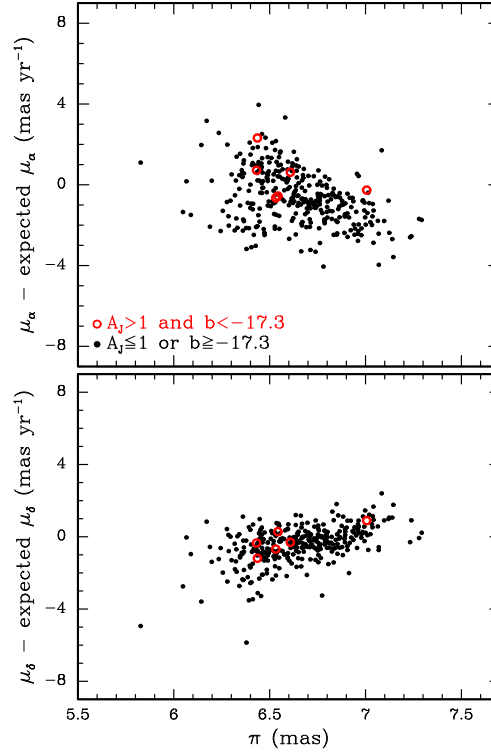


FIG. 12.— Proper motion offsets versus parallax for members of Corona Australis with  $\sigma_\pi < 0.5$  and  $\text{RUWE} < 1.6$  (Table 1). Different symbols are used for stars embedded in the cloud ( $A_J > 1$ ,  $b < -17.3^\circ$ ) and all other sources ( $A_J \leq 1$  or  $b \geq -17.3^\circ$ ).

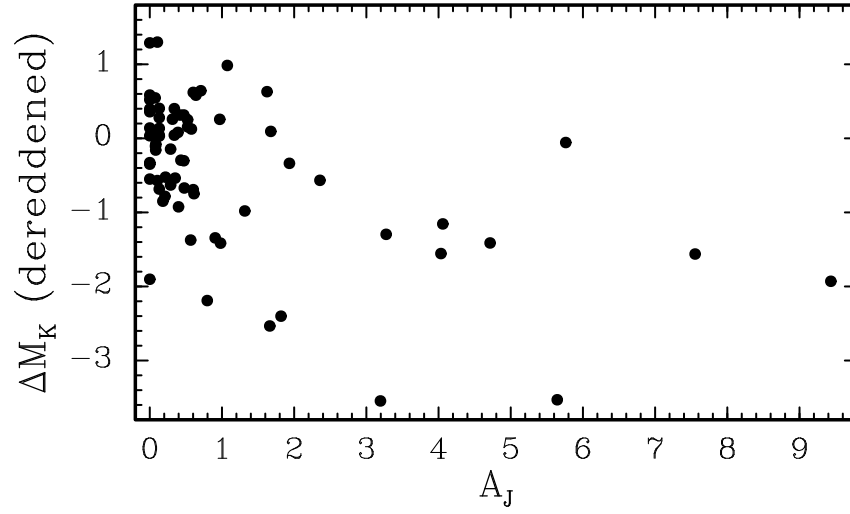


FIG. 13.—  $\Delta M_K$  versus  $A_J$  for members of Corona Australis that are near the cloud ( $b < -17.3$ ). The metric is defined as the difference between the extinction-corrected  $M_K$  and the median value for Upper Sco members at a given spectral type (Esplin et al. 2018). Higher values of  $\Delta M_K$  correspond to older ages.



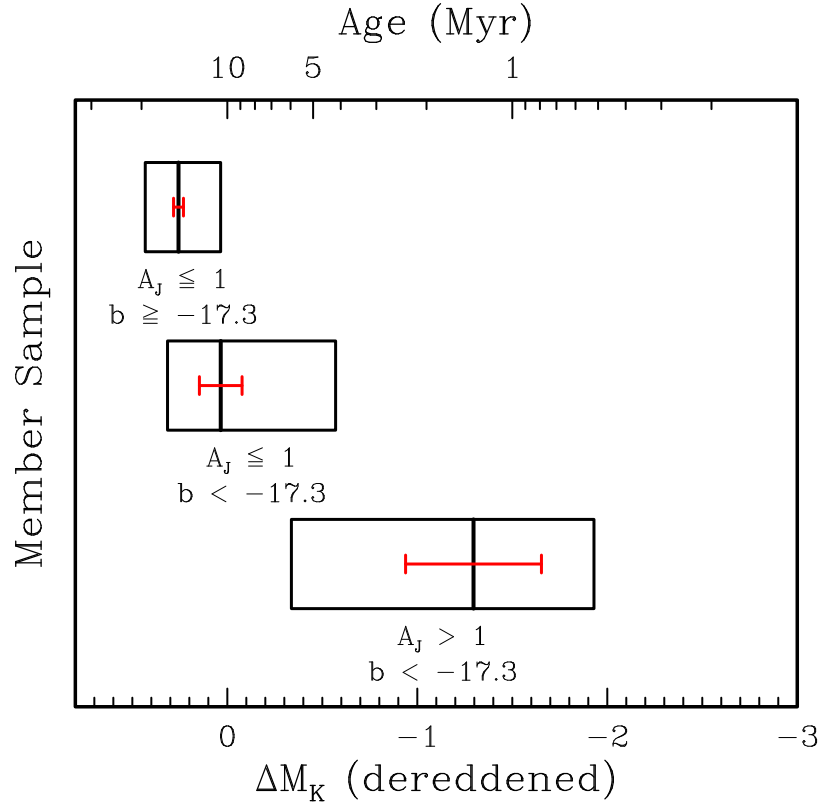


FIG. 14.— Box diagrams of the interquartile range of  $\Delta M_K$  calculated for individual members in three samples of Corona Australis members. The error bars represent the errors on the medians, which have been estimated via bootstrapping.

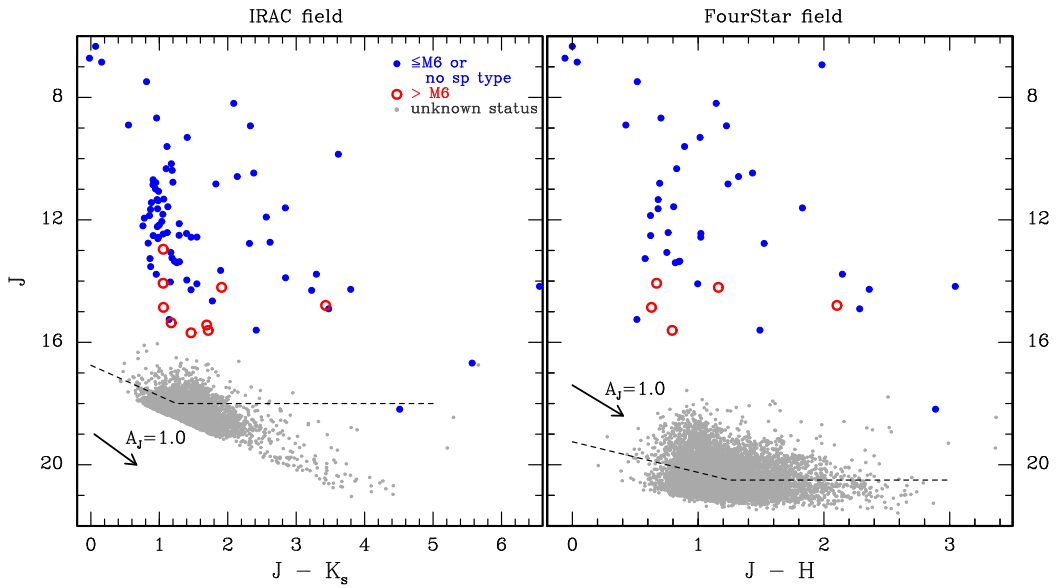


FIG. 15.— Color-magnitude diagrams of members of Corona Australis with spectral types  $\leq M6$  (blue points) and  $> M6$  (red circles) within the field imaged by IRAC in multiple epochs (left) and the field imaged by FourStar (right; see Figure 6). Sources with unknown status are indicated (gray points). The completeness limits for these data are marked (dashed lines).

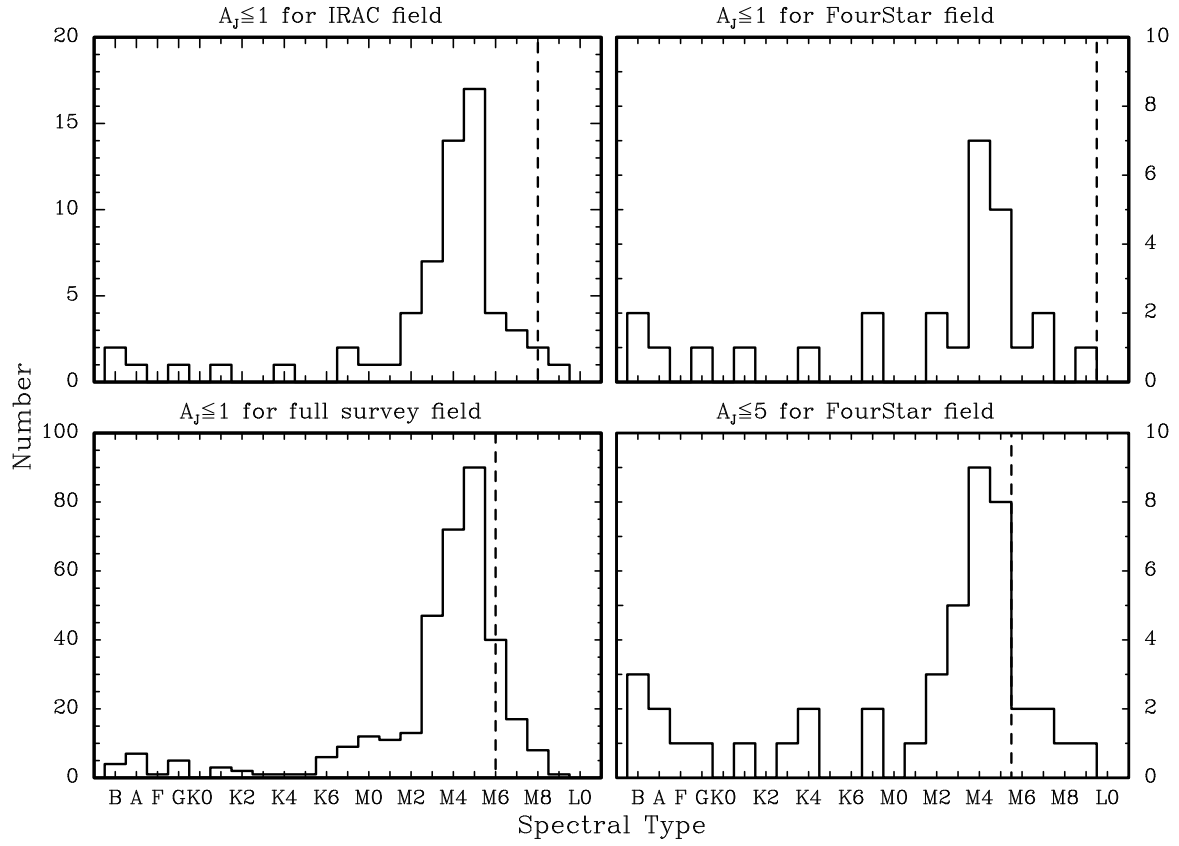


FIG. 16.— Histograms of spectral types for four samples of adopted members of Corona Australis. The completeness limits are indicated (dashed lines).

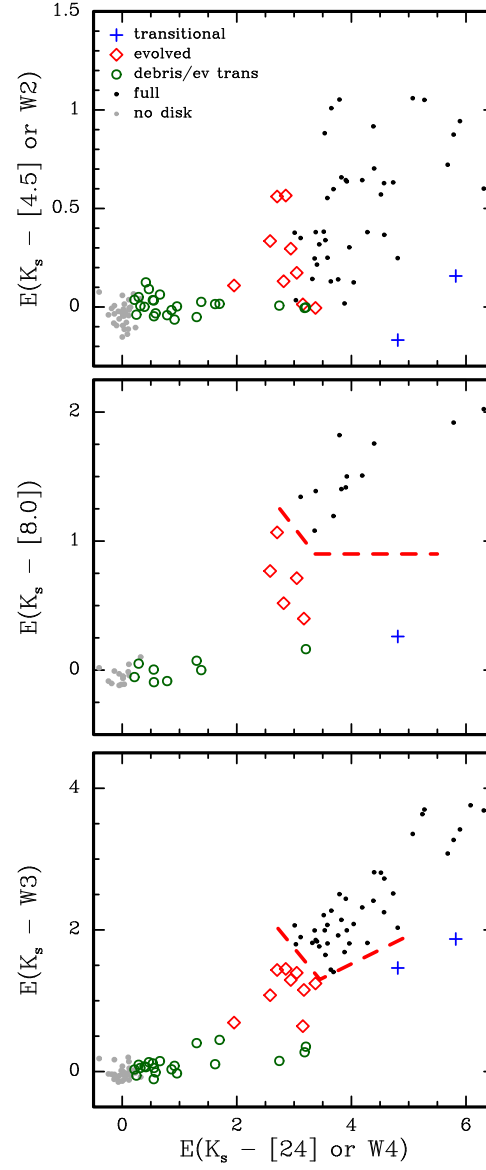


FIG. 17.— Extinction-corrected IR color excesses for adopted members of Corona Australis. If a source lacked  $[4.5]$  or  $[24]$  photometry, the  $W2$  or  $W4$  data is shown instead. The bottom two diagrams include boundaries that are used to distinguish full disks from disks in more advanced stages of evolution (dashed lines).